

# 3D toroidal physics: Testing the boundaries of symmetry breaking<sup>a)</sup>

Donald A. Spong<sup>b),c)</sup>

*Oak Ridge National Laboratory, Oak Ridge, Tennessee 37831-6169, USA*

(Received 9 March 2015; accepted 29 April 2015; published online 27 May 2015)

Toroidal symmetry is an important concept for plasma confinement; it allows the existence of nested flux surface MHD equilibria and conserved invariants for particle motion. However, perfect symmetry is unachievable in realistic toroidal plasma devices. For example, tokamaks have toroidal ripple due to discrete field coils, optimized stellarators do not achieve exact quasi-symmetry, the plasma itself continually seeks lower energy states through helical 3D deformations, and reactors will likely have non-uniform distributions of ferritic steel near the plasma. Also, some level of designed-in 3D magnetic field structure is now anticipated for most concepts in order to provide the plasma control needed for a stable, steady-state fusion reactor. Such planned 3D field structures can take many forms, ranging from tokamaks with weak 3D edge localized mode suppression fields to stellarators with more dominant 3D field structures. This motivates the development of physics models that are applicable across the full range of 3D devices. Ultimately, the questions of how much symmetry breaking can be tolerated and how to optimize its design must be addressed for all fusion concepts. A closely coupled program of simulation, experimental validation, and design optimization is required to determine what forms and amplitudes of 3D shaping and symmetry breaking will be compatible with the requirements of future fusion reactors.

© 2015 AIP Publishing LLC. [<http://dx.doi.org/10.1063/1.4921255>]

## I. INTRODUCTION

There is increasing interest in fusion devices that incorporate 3D, symmetry-breaking effects in their equilibrium state and in the development of new simulation methods that can address these effects. The motivations for introducing the 3D magnetic fields include plasma confinement and stability optimization (stellarators), plasma control (tokamak edge-localized and resistive wall instabilities), self-organized states (reversed field pinch single-helicity states), and engineering/economic constraints (limited number of toroidal field coils, asymmetrical particle/energy sources and non-uniform ferrous steel structure near the plasma).

Symmetry is a compelling and attractive feature for magnetic confinement systems. It assures the existence of magnetic flux surfaces, good particle confinement from conserved invariants of the motion, and simplifies analysis, for example, allowing many issues to be dealt with in some depth using analytic theory. However, deviations from symmetry have become integral to the operation and design of toroidal devices and constitute one of the major remaining areas for innovation that can lead to improved plasma performance. These 3D and symmetry-breaking effects complicate analysis, both with respect to theoretical modeling and in the interpretation of experimental diagnostics. The goal of this tutorial paper is to describe some of the new methods and the issues that are important to understanding the physics of 3D systems.

Symmetry-breaking effects have been present in magnetic fusion confinement systems for many years. Simple

magnetic mirror systems had, in principle, the highest inherent degree of symmetry (axial) of any devices, with deviations only present from coil positioning errors and construction tolerances. However, as these evolved to minimum-B and tandem mirrors, 3D effects were of interest<sup>1–4</sup> as configurations were changed to improve interchange stability and reduce end losses. The early tokamaks tested various levels of symmetry-breaking effects from different arrangements of toroidal field coils and non-symmetrical breaks in the conducting vacuum vessel. In some cases<sup>5</sup> (ORMAK) a large number, 56 toroidal field (TF) coils, were used in attempt to make ripple strength negligible; for other designs, such as the original Alcator device, non-axisymmetric groupings of coils led to relatively high ripple strengths of several percent even near the plasma center.<sup>6</sup> Discrepancies between ion temperatures derived from neutron measurements and those from charge exchange were attributed<sup>6</sup> to ripple losses. Existing and planned tokamak designs now typically use in the range of 18–22 TF coils. Tokamaks have recently introduced 3D coils for control of edge localized mode (ELM) instabilities; in ITER, toroidally non-uniform distributions of ferritic steel from test blanket modules and structures related to the neutral beams will introduce low levels of long toroidal wavelength ripple.<sup>7</sup> Stellarators have been 3D since their invention,<sup>8</sup> first in order to create vacuum rotational transform, and more recently to improve confinement, stability, bootstrap current consistency, and turbulent transport. Some of the earliest stellarators had issues with poor flux surfaces and confinement<sup>9</sup> caused by error fields and symmetry deviations; however, subsequent generations have improved flux surface integrity either by minimizing low order resonant ( $\dot{\iota} = 1/q = n/m$ ) field errors, designing in more shear in the rotational transform,

<sup>a)</sup>Paper UT2 1, Bull. Am. Phys. Soc. **59**, 325 (2014).

<sup>b)</sup>Invited speaker.

<sup>c)</sup>E-mail: spongda@ornl.gov

or, in the case of low shear configurations, avoiding low order rational surfaces altogether. Confinement has also been significantly improved by new optimization techniques, such as quasi-symmetry,<sup>10</sup> and quasi-omnigeneity,<sup>11,12</sup> which will be described in more detail later. Finally, reversed field pinches, while nominally toroidally symmetric in their earlier forms, have recently demonstrated spontaneous helical 3D states,<sup>13,14</sup> which have led to longer discharge durations and the generation of internal transport barriers. These equilibria have internal helical structures that are similar<sup>15</sup> to the “snake” structures that have been observed<sup>16</sup> and modeled<sup>17</sup> in the JET tokamak.

This evolving acceptance of 3D effects in magnetic fusion configurations is motivated by the fact that not all symmetry-breaking mechanisms count in the same way and plasma performance is tolerant of such effects up to some level. For example, long wavelength/resonant perturbations are generally more dangerous to the magnetic configuration than shorter wavelengths and phenomena such as collisions, turbulence, finite orbit width effects, ambipolar electric fields, and flow suppression of islands provide some shielding of 3D effects. In future fusion reactors, while the toroidal field coils will likely be further from the plasma (resulting in lower TF ripple), the effects of ports and other non-uniformity in the surrounding steel structures will introduce novel forms of ripple for which there is no current experience. 3D coils in reactors also are one of the few available tools for plasma control and optimization that do not involve large levels of recirculating power<sup>18</sup> (assuming such coils can be superconducting). However, the lower plasma collisionalities and larger energetic particle populations that will characterize reactors imply levels of symmetry-breaking that are tolerable in current experiments may need to be reexamined in light of reactor parameters. This motivates continued advances in 3D simulation tools and diagnostics.

Fortunately, as a result of the historical development of stellarators, and more recent interest in 3D effects in tokamaks and RFPs, a good basis has been established for these efforts. The purpose of this paper is to provide a tutorial introduction to current and historical work on 3D toroidal physics in tokamaks, stellarators, and reversed field pinches. A basic toolkit of methods that can be applied in a unified way to all 3D systems will be described and current research trends discussed that are expected to lead to improvements in the modeling and simulation of these systems. The topics of 3D symmetries, design of 3D configurations, equilibrium, confinement and stability will be covered, with various examples given in each area. This is not intended to be a comprehensive review. Excellent reviews<sup>18–21</sup> for those seeking more depth in this area have recently been published.

This tutorial paper is organized as follows. In Sec. II, the extended forms of symmetry (field period and stellarator symmetry) that are relevant to 3D configurations are described. In Sec. III, the characterization of 3D systems and the design methods used to synthesize them are discussed. Section IV presents a basic formulation of the 3D plasma equilibrium problem and describes computational approaches that are being used to obtain equilibria.

Section V first discusses methods for analyzing single particle confinement and then outlines their application to configuration optimization, energetic particle transport, neoclassical transport, and anisotropic transport in chaotic field line regions. Finally, Sec. VI describes the stability analysis of 3D systems, including energetic particle instabilities, micro-turbulence, stability of the 3D tokamak edge, and MHD stability of stellarators, with discussions included of possibilities for stability optimization.

## II. EXTENDED FORMS OF SYMMETRY FOR 3D SYSTEMS

The most general definition of symmetry is that an object observed from different viewpoints looks the same. Magnetic confinement systems such as simple mirrors and idealized axisymmetric tokamaks possess such symmetries about a single axis of rotation. This is denoted as continuous symmetry since such systems look the same for arbitrary angular rotations about a symmetry axis. The next level of symmetry is field period symmetry; this characterizes idealized stellarators and rippled tokamaks. This is a discrete form of axial symmetry and implies that the device will only look the same if it is rotated through discrete angular increments. For example, the LHD stellarator,<sup>22</sup> with 10 field periods, would appear the same if rotated through a toroidal angle of 36°, a tokamak with 20 planar toroidal field coils, an angle of 18°, etc. The lowest form of field period symmetry would be one field period. This only implies periodicity over a  $2\pi$  change in toroidal angle, which all toroidal devices must conform to. Recent examples of devices with one field period are ITER with the effects of ferrous materials in the test blanket modules (TBM) taken into account<sup>7</sup> (isolated to a 120° sector of the tokamak) and DIII-D with TBM simulation coils<sup>23</sup> (localized to one toroidal location). Also, if random field errors are taken into account, one field period would be the default degree of symmetry for a toroidal device. At the other extreme, a perfectly axisymmetric tokamak can be thought of as having an infinite number of field periods. In Figure 1, examples of (a) continuous and (b) discrete symmetry are given. From a computational perspective, devices with higher field periods require less data to achieve the same degree of resolution, since equilibrium quantities only need be represented over one field period; alternately, in Fourier representations, this implies that expansions in toroidal mode number go in increments of the field period. Low field period configurations are then the most challenging to model, even in the case when the 3D effects are weak. Examples of these include compact stellarators, tokamaks with ELM coils, and tokamaks with TBM effects.

The second form of symmetry that characterizes toroidal systems is known as “stellarator symmetry.” This can be thought of as a generalization of reflection symmetry to helical systems. For stellarators, this implies an observer will see the same view looking one way around the torus as looking the opposite direction and standing on one’s head [i.e., quantities at a point ( $R, \zeta$ , and  $z$ ) are the same as at ( $R, -\zeta$ , and  $-z$ ), where  $R$  is the major radius,  $\zeta$  is the toroidal angle, and  $z$  is the elevation]. For tokamaks, this type of symmetry

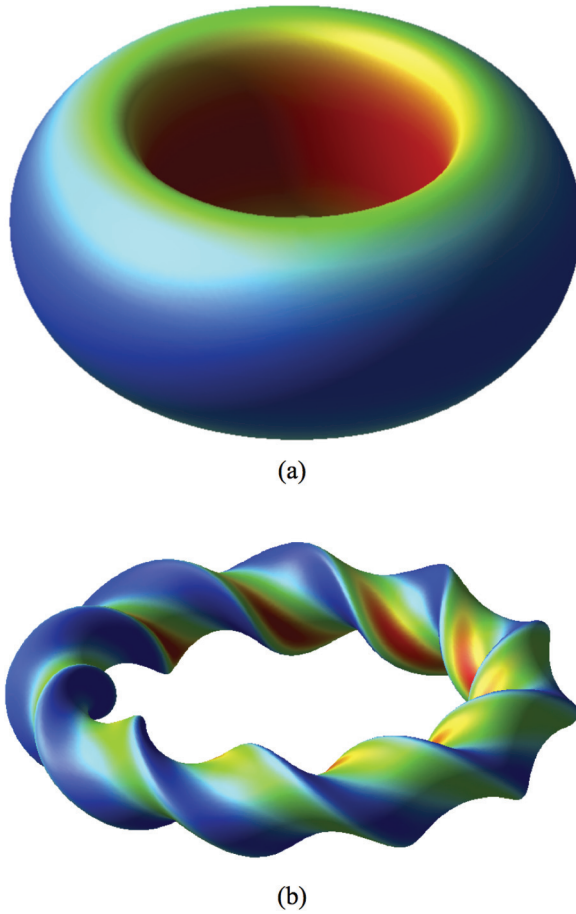


FIG. 1. (a) Axisymmetric tokamak with continuous rotational symmetry; (b) 10 field period stellarator with discrete symmetry. Colors indicate magnetic field strength.

implies up-down symmetry for each cross-sectional slice at a fixed toroidal angle. Stellarator symmetry for 3D systems is not known to have any direct physics advantages,<sup>24</sup> but simplifies the analysis of such systems in the sense that only half of the volume needs to be taken into account in representations of equilibrium magnetic fields, coil geometries, etc. For example, in Fourier space, the magnetic field magnitude can be expanded as a series in  $\cos(m\theta - n\zeta)$ , without the need to include  $\sin(m\theta - n\zeta)$  terms. Since most stellarators have tried to adhere to this type of symmetry (i.e., at least in the idealized limit, not including field errors), many of the modeling tools originally developed for stellarator physics assume stellarator symmetry. Tokamaks, routinely deviate from stellarator symmetry by tolerating up-down asymmetries, as for example, are the case with single-null divertors. Increasingly, stellarator analysis tools are being generalized to be applicable diverted tokamaks with 3D effects that violate stellarator symmetry.

### III. SYNTHESIS AND DESIGN OF 3D CONFIGURATIONS

The design techniques for 3D configurations have evolved from largely intuitive/semi-analytical approaches that begin with multipolar helical or window-pane coil concepts to computationally intensive optimization methods in high dimensional design spaces. The former is characteristic

of the early stellarator designs and more recent tokamak 3D control coil designs; the computational approach has been used first for the W7-AS,<sup>25</sup> W7-X,<sup>26</sup> and HSX<sup>27</sup> devices and for recent modular stellarator design efforts. One of the strengths of 3D shaping is the very large design space that is available. The available 3D plasma shaping parameters are limited by the fact that field structures that can be produced by collections of magnetic dipoles outside the plasma drop off strongly as one moves into the plasma. Since approximately a 1-m separation is needed in a reactor between the coils and the plasma (for the blanket and shield) and engineering constraints will set some minimum radius of curvature for coils, this precludes producing short wavelength variations in equilibrium magnetic fields beyond some level. Estimates have been made<sup>28</sup> of the maximum number of parameters that can effectively be used by performing SVD (singular value decomposition) of coil-to-plasma shaping transfer functions; these studies have concluded that  $\sim 30\text{--}40$  shape parameters should be available. However, this is still a very large design space compared to axisymmetric tokamaks, where the 2D shape is typically determined by 3–4 parameters (aspect ratio, elongation, triangularity, indentation, etc.). For example, if one was to perform a thought experiment by arbitrarily quantizing each shape parameter into 10 levels, 2D systems (i.e., axisymmetric tokamaks) would have about  $10^4$  possibilities, while 3D systems (optimized stellarators) would have  $10^{40}$  possibilities. While many of these may be of no interest or redundant, even if only a small fraction are attractive, the size of the 3D design space remains quite large.

Currently, the most advanced methods for 3D design use numerical optimization methods, such as Levenberg-Marquardt,<sup>29</sup> genetic evolution,<sup>30</sup> or differential evolution.<sup>31</sup> Since 3D equilibria are uniquely determined by the outer flux surface shape in combination with the pressure profile plus either the rotational transform or plasma current profiles, one approach for designing 3D systems has been to vary the shape of the outer magnetic flux surface to minimize a range of physics and engineering target functions.<sup>32</sup> The profile functions can either be fixed or varied. The target functions typically would include particle confinement, transport, MHD stability, micro-turbulence, aspect ratio, etc. Once a sufficiently optimized configuration is obtained, a set of modular coils can then be derived<sup>33</sup> on a specified coil-winding surface surrounding the plasma. These are first obtained as continuous sheet currents, and then steps are taken to discretize the current distribution, resulting ultimately in 3D current paths that can be practically realized as coils. Due to the fact that the discretized coils may not precisely reproduce the original optimized surface, tradeoffs must be made and the process may go through a succession of iterations. A more recent approach has been directly optimizing from the coil-set,<sup>34</sup> with its geometry described either by discrete points on the coils or by mathematical functions, such as splines or Fourier series. In this method, the external magnetic fields produced by the coils are used to compute a 3D plasma free-boundary equilibrium, physics/engineering target functions are calculated, the coil geometry and currents are varied, the equilibrium and targets are recomputed,

and the cycle continues until a desired configuration is found.

There are a variety of ways to categorize 3D systems. For this section, the focus will be on methods used for producing rotational transform, since this is the first basic issue to be considered in a design effort. The earliest stellarators were designed with the goal of producing all of the needed rotational transform from the vacuum magnetic fields, allowing steady-state confinement without the need for externally driven plasma currents. The two primary methods for achieving this (other than internal toroidal plasma current) have been recognized<sup>8,20,35</sup> since the earliest development of stellarators: (a) using a helical magnetic axis, which introduces torsion, or (b) keeping the magnetic axis planar, but helically rotating the outer magnetic surfaces. In Figure 2, these approaches are shown, along with the case of a 3D tokamak, which uses only internal current to produce transform; here, TJ-II<sup>36</sup> given as an example of (a) and LHD<sup>22</sup> as an example of (b). The rotational transform profiles ( $\dot{\psi} = 1/q$ , where  $q$  is the tokamak safety factor) associated with the configurations of Figure 2 are given in Figure 3. More recent optimized stellarators may use some mixture of these two approaches. Even devices such as LHD with perfectly planar magnetic axes in the vacuum state will tend to acquire helical deformations in the axis as the plasma beta is increased. As can be seen, the two stellarators produce rotational transform profiles that increase in going outward from the magnetic axis,

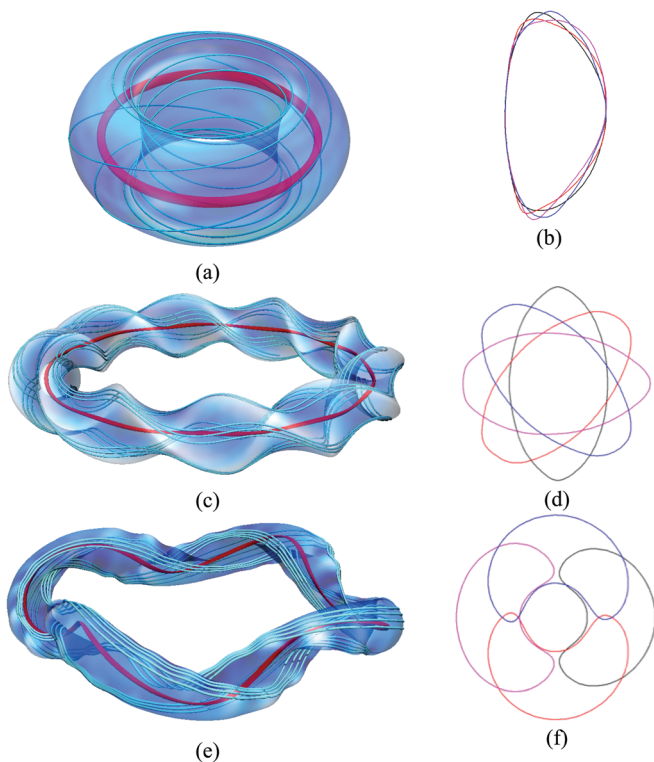


FIG. 2. Outer flux surfaces (transparent blue), magnetic field lines (light blue), and magnetic axis (red) for (a) tokamak with ELM coils, (c) LHD stellarator, (e) TJ-II stellarator. Flux surface 2D shapes at  $\phi = 0$  (black),  $\phi = 0.5\pi/N_{fp}$  (red),  $\phi = \pi/N_{fp}$  (magenta),  $\phi = 0.75\pi/N_{fp}$  (blue) for (b) tokamak with ELM coils ( $N_{fp} = 3$ ), (d) LHD stellarator ( $N_{fp} = 10$ ), (f) TJ-II stellarator ( $N_{fp} = 4$ ). For the tokamak case, 3D effects were enhanced by a factor of 10.

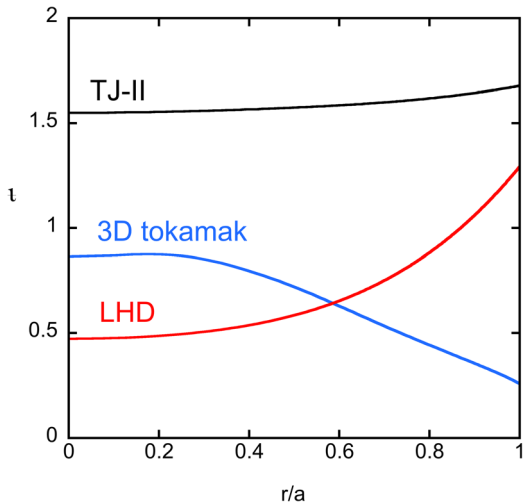


FIG. 3. Rotational transform ( $\dot{\psi} = 1/q$ ) profiles for the TJ-II, tokamak with ELM coils, and LHD cases given in Figure 2.

while standard tokamak transform profiles decrease in going toward the plasma edge (i.e.,  $q$  increases going outward from the axis). An intuitive way to understand how 3D shaping can produce vacuum rotational transform has been introduced,<sup>18</sup> noting the analogy between magnetic fields (satisfying  $\nabla \cdot \mathbf{B} = 0$ ) and incompressible fluid flows (satisfying  $\nabla \cdot \mathbf{v} = 0$ ). An incompressible fluid flowing through these shapes would develop helical streamlines in a similar way as the magnetic field line trajectories follow helical paths. The two methods shown here for producing vacuum transform introduce separate tradeoffs. The helical axis approach is more efficient, leading to larger levels of transform (good for confinement of passing particles) at moderate aspect ratios and lower field periods. However, the planar axis approach produces more shear in the transform profile, which minimizes resonant magnetic island widths and can be stabilizing for some instabilities. As will be discussed further in Sec. V, both approaches have moderate to high levels of magnetic field ripple, which leads to higher levels of neoclassical transport and energetic particle loss. This has been improved by performing optimizations that target these physics characteristics. This approach has led to devices such as HSX,<sup>37</sup> W7-X,<sup>38</sup> QPS,<sup>41</sup> and NCSX.<sup>40</sup> Another issue is that within each approach, if one wants to increase the rotational transform, while preserving similar shaping within each field period, there are two equilibrium scaling laws:  $\dot{\psi}/N_{fp} = \text{constant}$  and  $\langle R \rangle / \langle a \rangle / N_{fp} = \text{constant}$  that are relevant. These imply that in order to increase transform one must increase the number of field periods and aspect ratio simultaneously.

An alternate design method that was identified for avoiding the trend to higher aspect ratio and/or stronger helical axis is the so-called hybrid approach, which accepts that some fraction of the transform can be produced by plasma current (but allowing a lower current level than in the equivalent tokamak) to augment the vacuum rotational transform present from 3D shaping. This plasma current could be provided either through the self-generated bootstrap current or driven by external sources (e.g., Ohmic, RF, and beams).

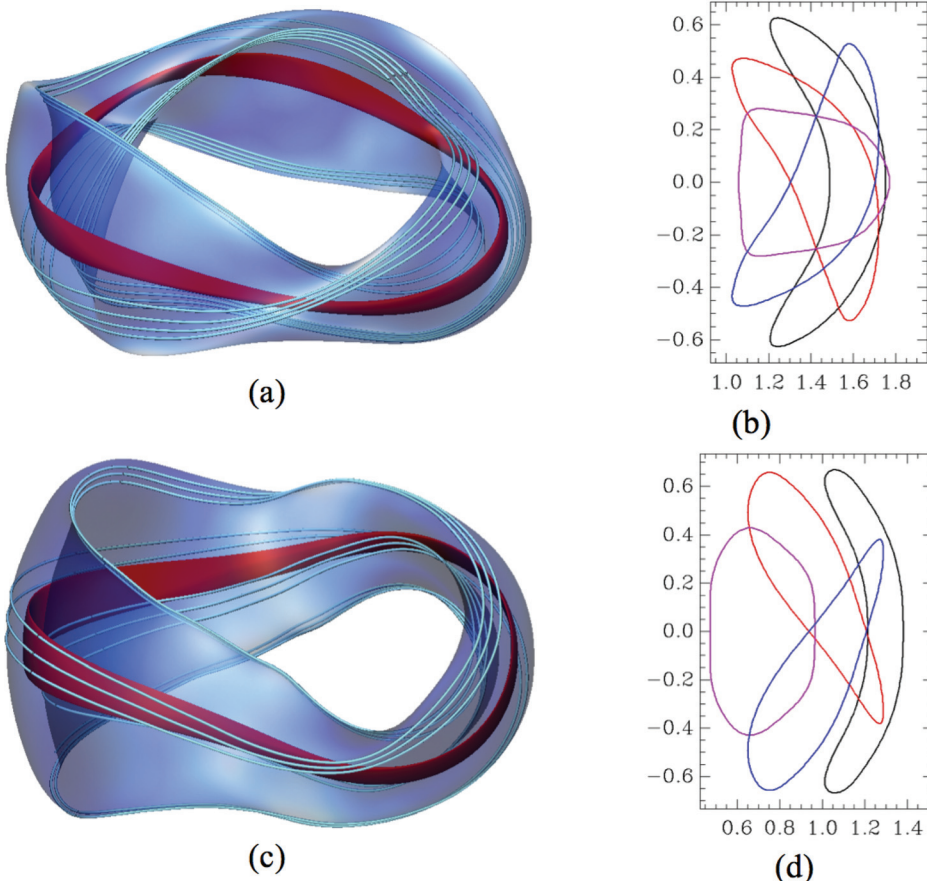


FIG. 4. Outer flux surfaces (transparent blue), magnetic field lines (light blue), and magnetic axis (red) for compact stellarator hybrids (a) NCSX, (c) QPS. Flux surface 2D shapes at  $\phi=0$  (black),  $\phi=0.5\pi/N_{fp}$  (red),  $\phi=\pi/N_{fp}$  (magenta),  $\phi=0.75\pi/N_{fp}$  (blue) for (b) NCSX ( $N_{fp}=3$ ), and (d) QPS ( $N_{fp}=2$ ).

This concept is used in the CTH experiment<sup>39</sup> and was incorporated to varying degrees in the NCSX<sup>40</sup> and QPS<sup>41</sup> compact stellarator projects. Their characteristic flux surface shapes and cross sections are shown in Fig. 4 with the associated transform profiles given in Figure 5. As indicated, relatively low aspect ratios were achieved with moderate levels of rotational transform. The examples shown have stellarator-like shear in the iota profiles, but configurations were also found with tokamak-like shear. The QPS design incorporated a racetrack shaped 2-field period helical axis, while NCSX had closer to a planar axis in a 3-field period design.

Another approach is to use tilted planar toroidal field coils.<sup>42,43</sup> In the case of two field periods (the CNT device at Columbia University),<sup>44</sup> this produces vacuum rotational transform. As more tilted coils are added (as in the Proto-Circus device, also at Columbia),<sup>45</sup> a configuration results that can be considered a “rotational transform amplifier.” i.e., while it may not have vacuum rotational transform, as plasma current is added it produces higher levels of rotational transform (lower  $q$ ) than a similar tokamak at the same aspect ratio. Calculations have shown that these configurations also can offer lower magnetic field ripple<sup>46</sup> than the equivalent tokamak with the same number of TF coils.

The 3D reversed field pinch relies on inductively-driven currents and spontaneous MHD self-organization to produce a single-helicity configuration<sup>13,14</sup> with a helical magnetic axis having low levels of  $q$  (very high levels of rotational transform) that can pass through zero and reverse near the plasma edge. These configurations derive most of their

rotational transform from plasma currents, with only small components from the 3D effects; however, they have demonstrated improved plasma sustainment and internal transport barriers with the spontaneous 3D equilibrium states. Typically, the internal flux surfaces of single-helicity RFPs are strongly 3-dimensional near the axes, but then become more axisymmetric near the plasma outermost surface.

In the case of tokamaks, all rotational transform is produced from plasma currents. 3D perturbations are used for other purposes and can be either introduced intentionally (in the case of ELM coils) or of necessity (TF ripple, TBMs,

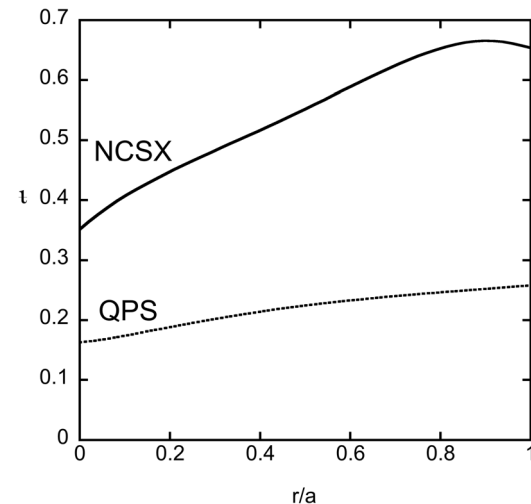


FIG. 5. Rotational transform ( $\iota=1/q$ ) profiles for the NCSX, and QPS cases given in Figure 4.

ferritic materials, etc.). In the case of ELM coils, the so-called “window-pane” coils, as shown in Figure 6, are added; these surround the plasma and produce field components that are approximately normal to the plasma outer surface. The purpose of these coils is to locally break-up the outer flux surfaces, forming an edge stochastic layer, as illustrated in the right-hand image in Figure 6; the goal is to limit the strong plasma pressure gradients in the pedestal region. This can suppress ELM instabilities, which, in larger systems such as ITER and reactors, will need to be avoided since they can lead to severe transient heat loads on plasma-facing components. Figure 7 shows the types of perturbations in the outer magnetic flux surface of a tokamak that (a) ELM coils can produce and (b) TF ripple + TBMs (test blanket modules) can produce.

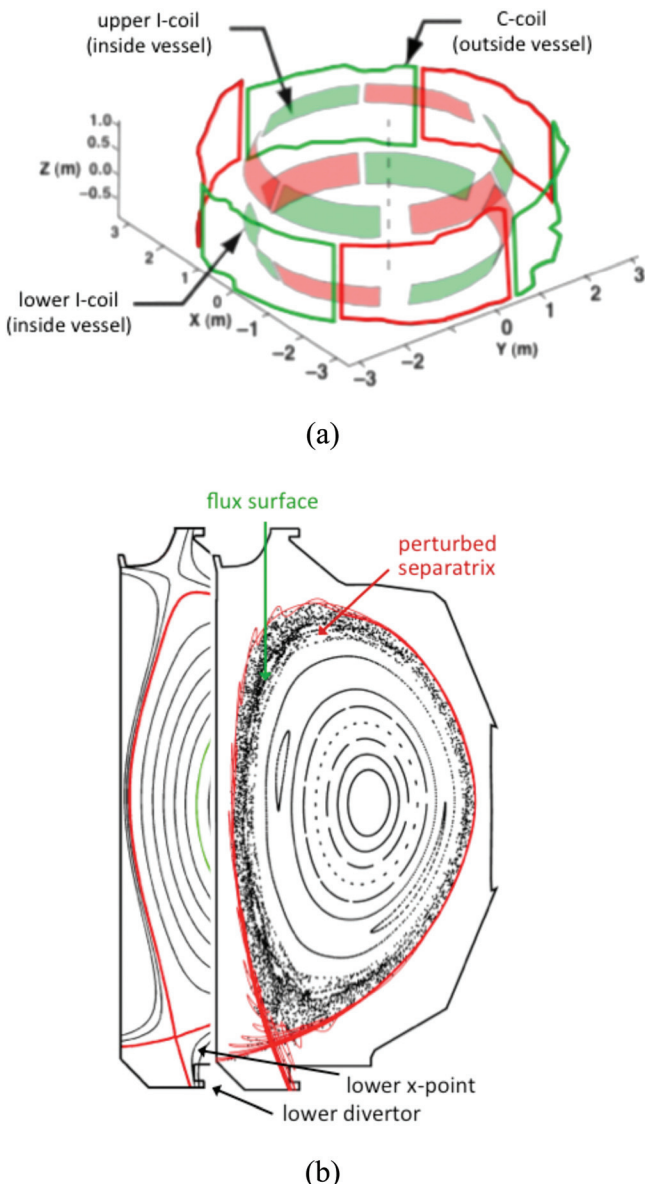


FIG. 6. (a) Arrangement of windowpane coils used in DIII-D to create stochastic edge regions (unpublished figure reprinted with permission from Todd Evans), (b) Stochastic edge and inner magnetic flux surface region with islands produced by ELM coils. Underlying background figure shows flux surfaces of axisymmetric equilibrium (unpublished figure reprinted with permission from Andreas Wingen).

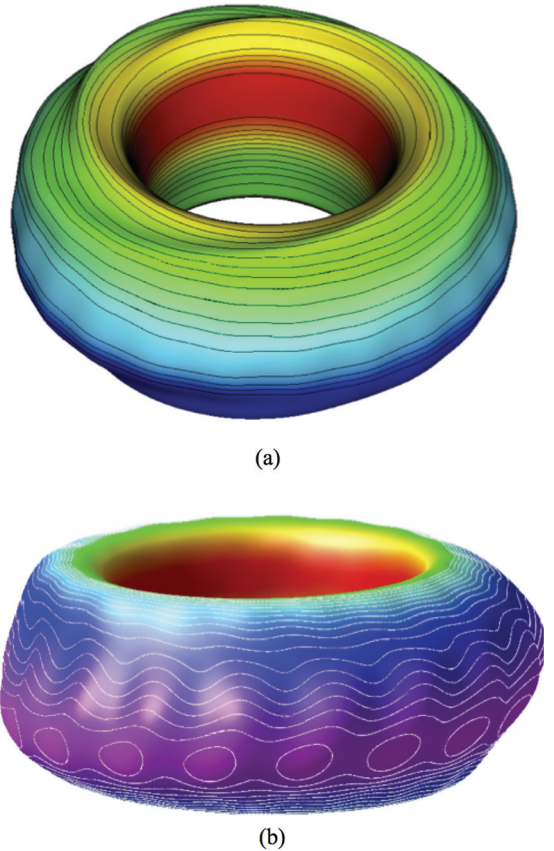


FIG. 7. Two forms of 3D tokamak outer flux surface perturbations (colors and contour lines indicate magnetic field strength): (a) distortion caused by ELM suppression coils; (b) distortions from toroidal field ripple plus test blanket module effects (3D effects in these figures magnified by a factor of 50).

modules) can produce. Here, the colors and contour lines indicate magnetic field strength and the non-axisymmetric shape changes have been enhanced by a factor of 50.

#### IV. 3D TOROIDAL EQUILIBRIUM MODELS

Accurate 3D toroidal magnetic equilibria, self-consistently including the effects of the plasma pressure and currents, form the basis for all subsequent plasma physics analysis and modeling. While, as will be explained, 3D equilibria offer a number of unique challenges, there are now efficient computational tools available that provide equilibria over a hierarchy of approximations and function in nearly as routine a manner as axisymmetric tokamak equilibrium models.

The basic equations for 3D equilibria are the force balance, Ampere's law, and absence of magnetic monopoles

$$\vec{F} = \vec{\nabla}p - \vec{J} \times \vec{B} = 0, \quad (1)$$

$$\mu_0 \vec{J} = \vec{\nabla} \times \vec{B} \Rightarrow \vec{\nabla} \cdot \vec{J} = 0, \quad (2)$$

$$\nabla \cdot \vec{B} = 0. \quad (3)$$

These are equivalent to the variational form,  $\delta W = 0$  derived by Kruskal and Kulsrud,<sup>47</sup> where

$$\delta W = \int \left( \frac{|B|^2}{2\mu_0} + \frac{p}{\gamma - 1} \right) d^3x. \quad (4)$$

This integral form allows weak solutions (i.e., without fully resolving sheet currents that are present at rational surfaces) to be obtained through minimization of  $\delta W$ , and has been quite useful in development of equilibrium solvers.

The 3D equilibrium problem was first analyzed mathematically by Grad<sup>48</sup> and Lortz.<sup>49</sup> They determined that the existence of solutions of Eqs. (1)–(3) could only be guaranteed for the special cases of closed field line (bumpy torus) and axisymmetric (tokamak) systems. This issue continues to be pursued, with recent work by Weitzner<sup>50</sup> showing that equilibria could be obtained in a simple topological torus model through expansions in a small parameter measuring the deviations of pressure surfaces from a simple nested surface structure. Basic differences between 2D and 3D equilibria arise from the characteristics of the governing partial differential equations (PDE). Axisymmetric equilibria are described by the Grad-Shafranov equation, which is a nonlinear elliptic 2D PDE, and there are a number of accurate, efficient solution methods available, along with many useful analytic approximations. 3D equilibria, however, lead to a mixed nonlinear hyperbolic/elliptic system. As discussed in Ref. 50, equation systems of this type only appear in a few other applications (transonic flow, lower hybrid wave propagation) and general solution methods are relatively undeveloped. 3D magnetic equilibria also can have singular current sheets at rational surfaces, which lead to magnetic islands, and chaotic field line regions.

While these issues remain, the existence of the variational principle<sup>47</sup> has allowed the practical calculation of approximate 3D equilibria under a variety of model assumptions. The VMEC (Variational Moments Equilibrium Code)<sup>51</sup> model constrains the magnetic field lines to lie on nested flux surfaces and avoids the full resolution of the singular current sheets. The magnetic fields in VMEC are represented in the form

$$\vec{B} = \vec{\nabla}\zeta \times \vec{\nabla}\psi + \vec{\nabla}\theta \times \vec{\nabla}\chi, \\ \text{where } \zeta, \theta = \text{toroidal/poloidal angles}, \\ 2\pi(\psi, \chi) = \text{poloidal/toroidal magnetic fluxes}. \quad (5)$$

This form constrains  $\mathbf{B}$  to lie on flux surfaces (i.e.,  $\mathbf{B} \cdot \nabla\psi = \mathbf{B} \cdot \nabla\chi = 0$ ). The minimization of the variational form (normally performed using a steepest descent algorithm) leads to equilibria without islands that do not fully resolve singular currents, but generally prove to be reasonable approximations to more exact solutions that relax such constraints. The other feature of VMEC is that it is an inverse equilibrium solver; i.e., it solves for the coordinate locations or geometric shapes of the magnetic surfaces as a function of magnetic flux and toroidal/poloidal angles in contrast to the direct approach, which would solve for the magnetic fields as a function of position. This allows a special choice of poloidal angle to be made that is optimized for good resolution/convergence. VMEC is now extensively used as the basis for most stellarator physics models and

optimizations and can function in both fixed<sup>51</sup> and free boundary<sup>52</sup> modes. It also has been validated against experimental measurements of flux surface shapes in stellarators<sup>53</sup> as the plasma  $\beta$  was varied. Versions of VMEC with anisotropic pressure<sup>54</sup> and toroidal flows<sup>55</sup> have been developed. An important application of VMEC has been 3D equilibrium<sup>56,57</sup> reconstruction. This process follows a similar hierarchy as configuration optimization, except that in place of physics/engineering target functions, the deviations between various experimental measurements (i.e., magnetic probes, profile diagnostics, etc.) and those predicted from the equilibrium calculation are targeted for minimization. The goal is a reconstruction that provides a best fit, taking into account all available information about the discharge.

The existence of singular current sheets and magnetic islands in both stellarators and 3D tokamaks has stimulated development of a number of models beyond VMEC. These aspects of 3D equilibria become especially important as the plasma  $\beta$  is increased. The PIES (Princeton Iterative Equilibrium Solver)<sup>58</sup> is a direct solution approach based on the Picard iteration algorithm. PIES iterates between computing currents and magnetic fields, requiring some degree of averaging over old and new solutions to maintain numerical stability. The HINT-2 model<sup>59</sup> is also a direct solver, iterating between maintaining pressure constant along field lines, calculating magnetic fields, and currents. HINT-2 uses rotating helical coordinates, which are an efficient representation for heliotrons. The SPEC model<sup>60</sup> uses a piecewise continuous approximation in the radial flux variable and avoids current sheets by setting the pressure gradient to zero on rational surfaces. SIESTA<sup>61</sup> is an extension of the VMEC variational approach to include islands. This is achieved by generalizing the VMEC independent variables to include a third magnetic field component normal to magnetic flux surfaces and a 3D pressure function. Small levels of resistivity are introduced to allow changes in magnetic field topology required for island formation. SIESTA utilizes a direct solver, based on coordinates determined by VMEC. A stellarator equilibrium and associated Poincaré plots indicating several island chains based on the SIESTA model is shown in Fig. 8.

For the case of tokamaks with weak 3D effects, various models have recently been developed. The simplest approach is to simply superimpose vacuum 3D magnetic fields on a conventional 2D equilibrium. This model has often been used for fast ion loss calculations in tokamaks with 3D perturbations. However, this approach misses self-consistent 3D modifications of flux surface shapes and plasma shielding/amplification effects. Beyond this, several models have used MHD equations to calculate the response of initially 2D tokamak equilibria to 3D fields that are imposed as inhomogeneous driving terms. Such models include the M3D-C1,<sup>62</sup> MARS-F,<sup>63</sup> and IPEC<sup>64</sup> solvers. MARS-F and IPEC are linear, single fluid, ideal codes, while M3D-C1 is resistive, can be run in either linear or nonlinear modes and can use either single or two fluid models with plasma rotation. Plasma rotation/flows can have important effects on limiting the size of magnetic islands.<sup>65,66</sup> Such models so far have only been applicable to tokamaks since they are based on the assumption of small perturbations away from axisymmetric

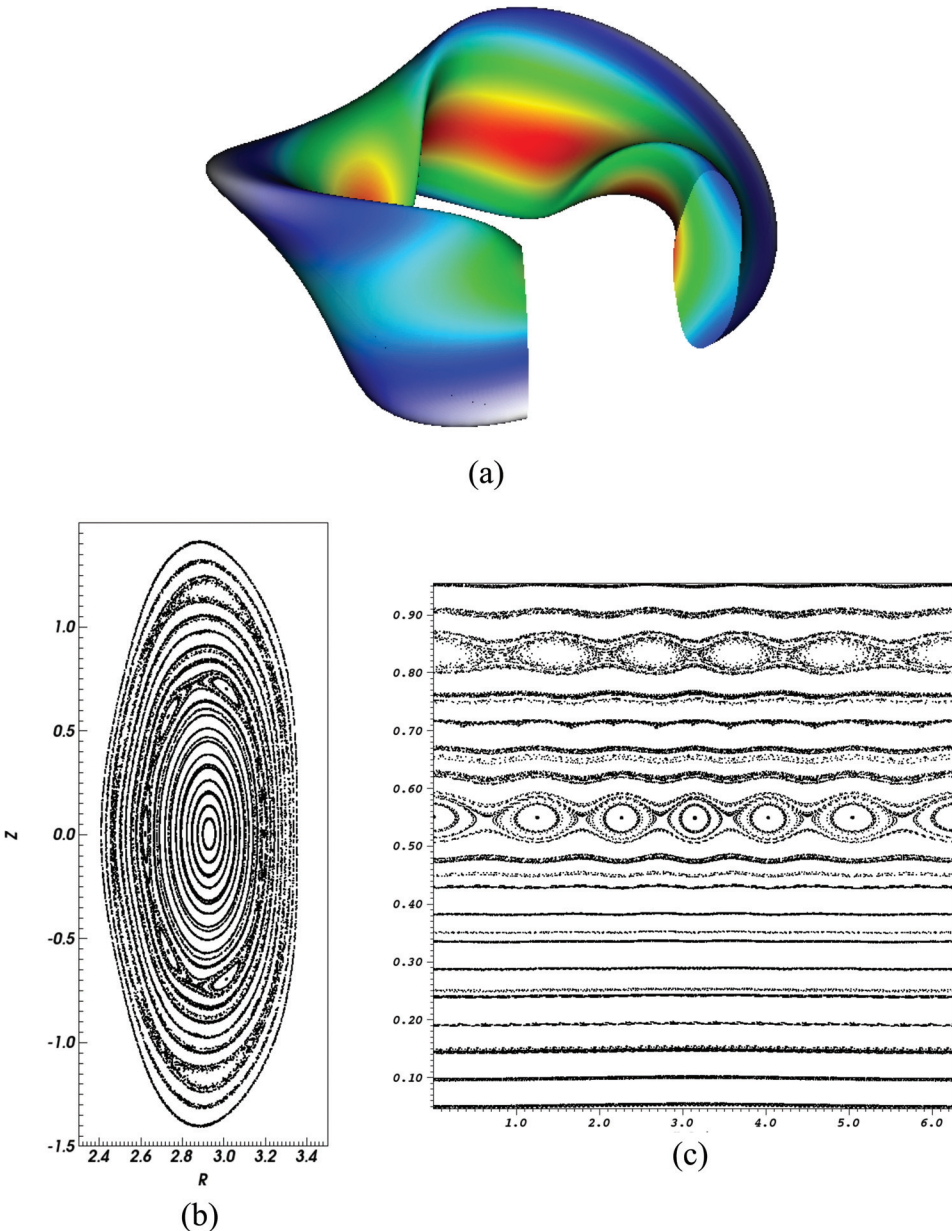


FIG. 8. 3D stellarator equilibrium with islands: (a) outer flux surface shape (color contours indicate magnetic field strength); (b) Poincare plot in  $R$ ,  $Z$  coordinate; (c) Poincare plot in  $s$ ,  $\theta$  coordinates [ $s = \sqrt{s}$  (normalized toroidal flux)].

equilibria. A code comparison/benchmark activity<sup>67</sup> has been initiated to compare predictions of a number of these models for 3D tokamak equilibria. A more recent comprehensive review<sup>68</sup> has compared results from IPEC,<sup>64</sup> MARS-F,<sup>63</sup> M3D-C1,<sup>62</sup> VMEC,<sup>51</sup> NSTAB,<sup>69</sup> and HINT-2.<sup>59</sup> Also, high resolution magnetic probe arrays have been recently installed<sup>70</sup> on DIII-D to provide experimental validation data for this activity. Calculation of 3D effects is especially important in the edge/pedestal and divertor scrape-off regions of tokamaks. Understanding transport in the edge/pedestal region and nearness to peeling-balloonning stability boundaries is critical to sustainment of enhanced confinement regimes and mitigating edge-localized instabilities. The goal of 3D perturbations from external ELM control coils is to regulate the pedestal pressure gradients so that ELMs are suppressed without destroying confinement. In future, larger tokamaks ELMs can transfer large transient heat loads to plasma-facing components and will need to be suppressed. The observations that as 3D fields are applied

some experiments see ELMs suppressed,<sup>71,72</sup> while others see ELM triggering,<sup>73</sup> make the pedestal region both of great interest, but also remains a significant challenge for modeling. In the outer divertor scrape-off region, 3D fields lead to strike point splitting,<sup>74</sup> novel structures known as homoclinic tangles<sup>75–78</sup> and possible loss of detachment at the divertor plates. Due to the extremely high scrape-off layer heat fluxes<sup>79</sup> anticipated in future tokamaks, good modeling of this region is also quite important. In addition to the substantial recent interest in modeling the edge and scrape-off regions, improved diagnostics<sup>80</sup> are now available, based on soft x-ray emissivity measurements. In order to resolve detailed features, energy filtering, reconstruction, and image analysis techniques are employed; also, by alternating the sign of the 3D magnetic field perturbations, differencing methods can be used to improve the contrast of the images. A recent example of a comparison<sup>81</sup> between the predicted effects of 3D perturbations, using the M3D-C1 model, and the emissivity measurements is shown in Fig. 9.

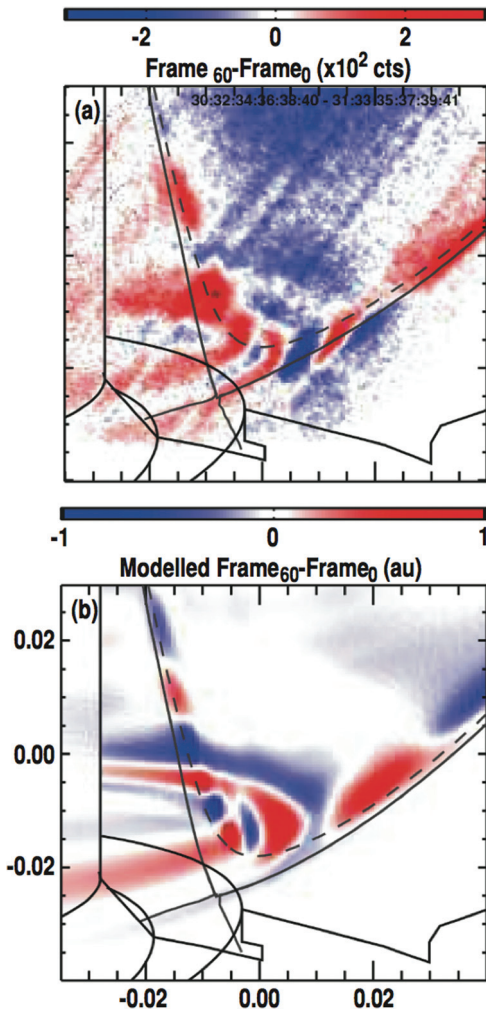


FIG. 9. Edge emissivity measurements with 3D perturbation coils in DIII-D (top) and MHD simulations using the M3D-C1 model. Reprinted with permission from N. M. Ferraro, T. E. Evans, L. L. Lao, R. A. Moyer, R. Nazikian, D. M. Orlov, M. W. Shafer, E. A. Unterberg, M. R. Wade, and A. Wingen, Nucl. Fusion **53**, 073042 (2013). Copyright 2013 IAEA.

## V. CONFINEMENT AND TRANSPORT IN 3D CONFIGURATIONS

### A. Orbit trajectory equations

With the breaking of toroidal symmetry, conserved invariants of particle motion, such as the canonical toroidal angular momentum ( $P_\phi$ ), are no longer available. In its place, the longitudinal invariant  $J = m \int v_{||} dl$  plays an analogous role as  $P_\phi$ ; bounce-averaged drift velocities can be derived from the invariant function  $J$  by:  $v_d = (1/e\tau_b B^2) \mathbf{B} \times \delta J$ , where  $\tau_b$  = bounce time =  $\int dl/v_{||}$ . The longitudinal invariant has been extensively used in the analysis of neoclassical transport, plasma stability, and as an optimization target function. If the energy and pitch angle are fixed, then contours of constant  $J$  represent the puncture points orbit trajectories onto a 2D constant toroidal angle plane analogous to the use of constant  $P_\phi$  contours to project tokamak orbits onto a toroidal slice. This property was used in one of the first applications<sup>82</sup> of the STELLOPT stellarator optimization code, and is known as quasi-omnigeneity. For systems with low levels of

rotational transform per field period,  $J$  can be simplified<sup>83</sup> to  $J^*$ , which replaces the integration along field lines with an integration along the toroidal angle at fixed values of poloidal angle and magnetic flux. The use of  $J$  for particle orbits in 3D systems is somewhat more complex than ( $P_\phi$ ) for several reasons. First, the evaluation of  $P_\phi$  is more straightforward (without the need to perform field line integrals), while  $J$  must be computed by performing integrals along field lines for a sequence of pitch angles (also for a range of energies, if an ambipolar electric field is included). Second, for configurations with multiple magnetic wells (trapping regions) along field lines, multiple branches of  $J$  must be considered and transition probabilities between them taken into account.<sup>84</sup> For these reasons, most recent studies of confinement in 3D configurations have been based on direct integrations of the particle equations of motion. The guiding center trajectory equations have been derived in both canonical and non-canonical formulations. These form the basis for many areas of simulation for 3D systems, including neoclassical transport, energetic particle confinement/stability, hybrid fluid/particle models, and gyrokinetics.

The canonical Hamiltonian approach<sup>85</sup> begins with the guiding center Hamiltonian

$$H_{GC} = \frac{1}{2}mv_{||}^2 + \mu B + e\Phi, \quad (6)$$

where  $m$ ,  $e$  = the particles mass and charge,  $B$  = the magnetic field strength,  $v_{||}$  = the velocity component parallel to field lines,  $\mu = mv_{\perp}^2/2B$ ,  $\Phi$  = the electrostatic potential. The conjugate momenta are defined by

$$P_\theta = m \frac{Iv_{||}}{B} + e\psi; \quad P_\zeta = m \frac{Gv_{||}}{B} - e\chi, \quad (7)$$

where  $I$ ,  $G$  = the toroidal/poloidal current functions;  $\psi$ ,  $\chi$  = the poloidal/toroidal magnetic flux functions. The particle equations of motion are then derived from  $\dot{\theta} = \partial H/\partial P_\theta$ ;  $\dot{\zeta} = \partial H/\partial P_\zeta$ ;  $\dot{P}_\theta = -\partial H/\partial \theta$ ;  $\dot{P}_\zeta = -\partial H/\partial \zeta$  and can be expressed as follows:

$$\frac{d\psi}{dt} = \frac{1}{D} \left( I \frac{\partial B}{\partial \zeta} - g \frac{\partial B}{\partial \theta} \right) \left( \mu + \frac{mv_{||}^2}{B} \right), \quad (8)$$

$$\frac{d\rho_{||}}{dt} = \frac{+ - \rho_{||}g'}{D} \dot{P}_\theta + \frac{\rho_{||}I'}{D} \dot{P}_\zeta, \quad (9)$$

$$\frac{d\theta}{dt} = \left[ \left( \mu + \frac{mv_{||}^2}{B} \right) \frac{\partial B}{\partial \psi} + e \frac{\partial \Phi}{\partial \psi} \right] \frac{\partial \psi}{\partial P_\theta} + eBv_{||} \frac{\partial \rho_{||}}{\partial P_\theta}, \quad (10)$$

$$\frac{d\zeta}{dt} = \left[ \left( \mu + \frac{mv_{||}^2}{B} \right) \frac{\partial B}{\partial \psi} + e \frac{\partial \Phi}{\partial \psi} \right] \frac{\partial \psi}{\partial P_\zeta} + eBv_{||} \frac{\partial \rho_{||}}{\partial P_\zeta}, \quad (11)$$

where  $D = e[G(\rho_{||}I' + 1 - I(\rho_{||}G' = +)]$ ;  $\rho_{||} = mv_{||}/eB$ .

Due to the form chosen for the Hamiltonian, the poloidal/toroidal angular coordinates ( $\theta$ ,  $\zeta$ ) have been chosen, so that the magnetic field lines in each magnetic flux surface are straight lines, and the particle trajectory equations only involve  $B$  (magnitude of the magnetic field) and its derivatives. Such coordinates are normally referred to as Boozer or

magnetic coordinates,<sup>85</sup> and result in the Jacobian =  $1/\sqrt{g} = B^2/(G + iI)\left(\frac{dy}{dp}\right)$ , where  $\rho$  is the magnetic flux surface label. This orbit model can also be extended<sup>86</sup> to include perturbation field components with the form  $\delta\mathbf{B} = \nabla \times (\alpha\mathbf{B})$ , as might be used to model magnetic islands or the presence of MHD or Alfvénic instabilities. The advantage of this choice is that less data are required to represent the magnetic field (i.e., only  $\mathbf{B}$  and its derivatives are required, rather than 3 components of  $\mathbf{B}$  with 3 derivatives of each component). Since this also means that fewer field evaluations must be made at each orbit step and memory requirements are smaller, it can increase efficiency of numerical trajectory calculations. Also, as will be described later, this form for the orbits allowed the recognition of the magnetic field structures known quasi-symmetries, in which the net radial drift over a bounce orbit could be brought to zero, leading to confinement characteristics similar to those of an axisymmetric tokamak. The disadvantage of the orbit model of Eqs. (7)–(10) is the need to transform to a particular choice of coordinates that are best suited to the case of equilibria with nested, closed flux surfaces. Methods for extending such coordinates outside of the last closed flux surface are discussed in Ref. 87. Also, Boozer coordinates are generally not optimal for representation of the geometries of plasma-facing structures, such as metallic walls, divertor plates, etc., at the plasma edge.

For these reasons, a set of non-canonical equations have been developed and are increasingly in use in applications, where one is interested in following particles outside the last closed flux surface. The following non-canonical orbit equations were derived by Littlejohn<sup>88</sup> from the variational action integral using Lie-transform perturbation techniques

$$\frac{d\vec{R}}{dt} = \frac{1}{B_{||}^*} \left( v_{||} \vec{B}^* + \vec{E}^* \times \hat{b} + \frac{\mu \hat{b} \times \vec{\nabla} B}{e} \right), \quad (12)$$

$$\frac{dv_{||}}{dt} = e(\vec{E}^* + \vec{R} \times \vec{B}^*) \mu \vec{\nabla} B, \quad (13)$$

$$\text{where } \vec{B}^* = \vec{B} + \frac{mv_{||}}{e} \vec{\nabla} \times \hat{b} \text{ and } \vec{E}^* = \vec{E} - \frac{mv_{||}}{e} \frac{\partial \hat{b}}{\partial t}. \quad (14)$$

These equations are coordinate-free and can be applied to whatever coordinate system is most convenient for the configuration under analysis.

The above two orbit models are based on the guiding center approximation. For energetic particle populations and regions of the plasma where parameters vary rapidly (e.g., edge and divertors), a number of models<sup>89,102</sup> are beginning to incorporate full Lorentz model orbits (i.e., including the rapid gyromotion). A related approach<sup>90</sup> is to use a hybrid of guiding center and Lorentz, with guiding center orbits followed in the central region of the plasma and then switching over to Lorentz orbits near the edge.

The orbit equations result in four ordinary differential equations (ODEs) per particle (six in the case of Lorentz), can be solved with a variety of methods (e.g., Runge-Kutta, variable time step, symplectic) and are readily adapted to parallel computers. For applications to transport and

energetic particle confinement, the time integration of the orbit trajectories is periodically paused and discrete Langévin (Monte Carlo) collisions<sup>91</sup> are applied to the velocity space variables in order to simulate drag and diffusion from Coulomb collision processes. 3D configurations introduce a larger number of orbit classes than axisymmetric systems. Several examples are shown in Figure 10 based on integrating the Hamiltonian orbit equations. Figures 10(a) and 10(b) display several orbit classes for the LHD stellarator, including passing, trapped-passing transitional (trapped in some field periods, but not others), and deeply trapped orbits that are localized to the magnetic field minima and precess around the torus following these minima. For these plots, an ambipolar electric field was present; otherwise the latter two classes of orbits would have been rapidly lost. Typically, the transitional and deeply trapped orbits have the highest loss rates due to uncompensated radial drifts and lead to the ripple neoclassical transport scaling ( $\sim 1/\nu$ , where  $\nu$  = collision frequency), which are unique to 3D systems. In Figures 10(c)–10(e), several orbit classes that are important for 3D tokamaks are displayed. This is an ITER case that has both TF coil ripple and ripple from iron in adjacent TBM. The red colored trajectories alternate between being locally ripple trapped and trapped over several ripple wells due to the interaction between the TF and TBM ripple effects. The purple orbit trajectory is a more normal trapped orbit, bouncing, and precessing within the  $1/R$  variation of  $|B|$ . However, due to the ripple, there is a slight jitter in the location of its banana tip locations. The banana tips do not remain attached to the original flux surface, as would be the case in a perfect axisymmetric system, and this leads to a form of ripple transport<sup>92</sup> that can be important for energetic particle species.

## B. Confinement optimization

The simplified dependency on  $B$  of the orbit equations in magnetic (Boozer) coordinates coupled with flexibility of 3D shaping has led to significant progress in confinement improvement in 3D systems. In order for optimization methods to target confinement, it was necessary to develop proxy functions that both were accurate reflections of the confinement physics and efficient to evaluate. An early approach to this problem was to target the extremal values (along the field lines) of the magnetic field strength. By recording the minimum and maximum values of  $B$  within a field period along each field line passing through a fixed toroidal angle cross section, 2D contours<sup>83</sup> of these  $B_{\min}$  and  $B_{\max}$  values could be plotted and compared with magnetic flux surfaces. By aligning the  $B_{\min}$  contours with adjacent flux surfaces, confinement of deeply trapped particles could be improved, while aligning  $B_{\max}$  contours with flux surfaces lessen the number of transitional, partially trapped/partially passing orbits. A subsequent concept was then to align contours of the longitudinal invariant,  $J$ , with flux surfaces. Such configurations are known as omnigenous<sup>93</sup> and offer the possibility that, by using evaluations of  $J$  at several different values of the pitch angle parameter  $\lambda = \mu/e$ , confinement could be improved over a larger region of velocity space than possible with the  $B_{\min}$  and  $B_{\max}$  optimizations. If exactly obtainable,

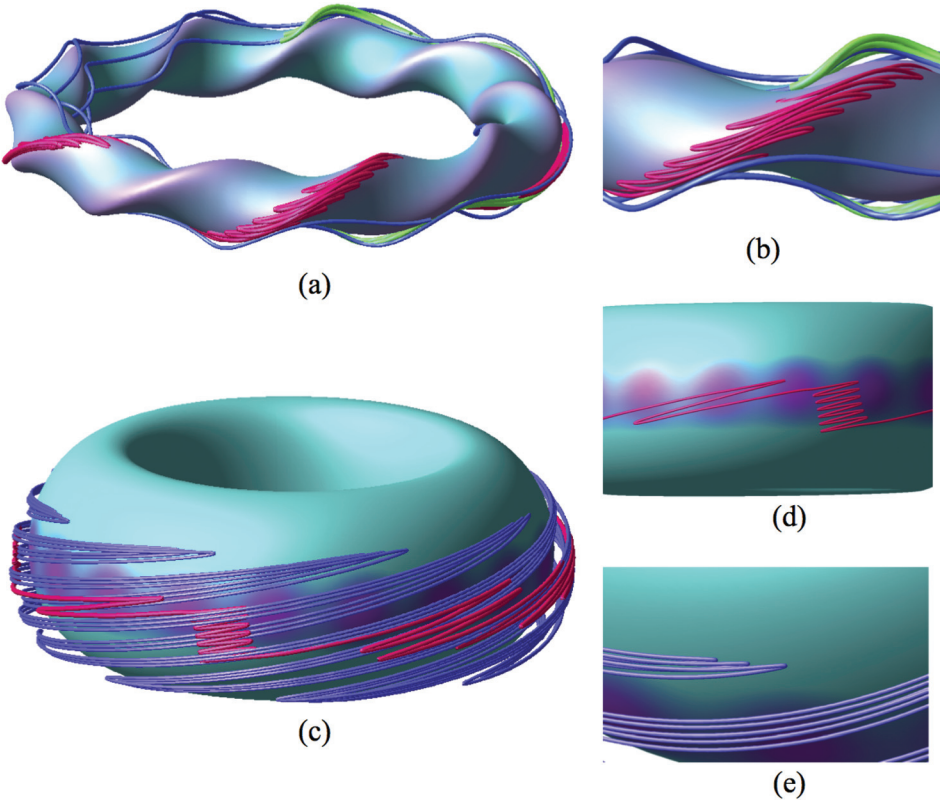


FIG. 10. Guiding center orbit trajectories for (a) a stellarator (red-deeply trapped, blue-passing, green-transitional) and (b) a tokamak with TF ripple and TBM effects (red-transitional trapped/passing, purple-trapped).

such an optimization strategy could reduce bounce averaged cross-field drifts to zero (they would still be locally non-zero) and remove<sup>94</sup> the ripple transport ( $D \sim 1/\nu$ ) regime scaling that is discussed in Sec. V D. The J optimization approach has also been shown to be equivalent to maintaining an equidistant separation<sup>95</sup> between contours of constant B within each flux surface. An example of applying the omnigenous optimization target is given in Ref. 32, where the related function  $J^*$ , which replaces the integration along field lines with an integration along toroidal angle, was used. Unfortunately, configurations that exactly satisfy the omnigenous criterion have not been found, but this optimization target has proven useful<sup>31</sup> in guiding the optimizer towards shapes that offer confinement improvement.

The next level of confinement improvement<sup>10</sup> is the quasi-symmetry approach; these require that the magnetic field has the form  $B = B(\rho, m\theta - nN_{fp}\zeta)$ , where  $m$  and  $n$  are integers,  $N_{fp}$  is the number of field periods,  $\rho$  is a flux surface label, and  $\theta, \zeta$  are the poloidal, toroidal angles in Boozer coordinates. Coordinate-free versions of this criterion have also been derived.<sup>96,97</sup> This magnetic field structure implies that an ignorable coordinate is present, leading to a conserved canonical momentum, similar to an axisymmetric tokamak. If this could be achieved, all of tokamak transport theory could be applied directly, through a procedure known as an isomorphic transformation.<sup>98</sup> Hypothetically, three separate quasi-symmetries can be considered: toroidal ( $n=0$ ), poloidal ( $m=0$ ), and helical ( $m, n$  both non-zero). However, it has not been possible to exactly achieve any of these symmetries in realistic devices and this fact has been supported by theoretical analyses.<sup>99</sup> Poloidal quasi-symmetry cannot be attained exactly in a toroidal system due to its

incompatibility with toroidal curvature. However, racetrack shaped two field period configurations, such as QPS,<sup>41</sup> and those with long straight sections joined by short curved regions can approach<sup>100</sup> this type of variation in the straight sections and reduce the losses of trapped particles. Quasi-toroidal symmetry is likely to some extent incompatible with vacuum transform since the only two known methods of creating vacuum transform (discussed in Sec. III) involve deviations in real space from toroidal symmetry. However, hybrid configurations, such as NCSX,<sup>40</sup> have achieved a good degree of quasi-toroidal symmetry by allowing a portion of the rotational transform to come from plasma current. A high degree of quasi-helical symmetry has been achieved in the design of the HSX device, which uses  $n=m=1$  and  $N_{fp}=4$ . In principle, other forms of quasi-helical configurations are possible by choosing different ratios of  $n/m$  than 1. As was the case with the omnigenous approach to optimization, targeting quasi-symmetry has yielded significant confinement improvement; even though these criteria have not been achieved in any exact sense.

### C. Energetic particle confinement

Confinement studies of the energetic particle (EP) component (i.e., beams, RF tails, alpha particles, runaway electrons) are an important application of the above orbit models in 3D systems due to concerns about loss of heating efficiency and the possible transfer of substantial energy fluxes onto plasma facing components. Since EPs are relatively collisionless, they are more sensitive to symmetry-breaking effects than thermal plasma components. For the case of tokamaks with 3D effects, the impact of magnetic field perturbations from localized test blanket modules have been

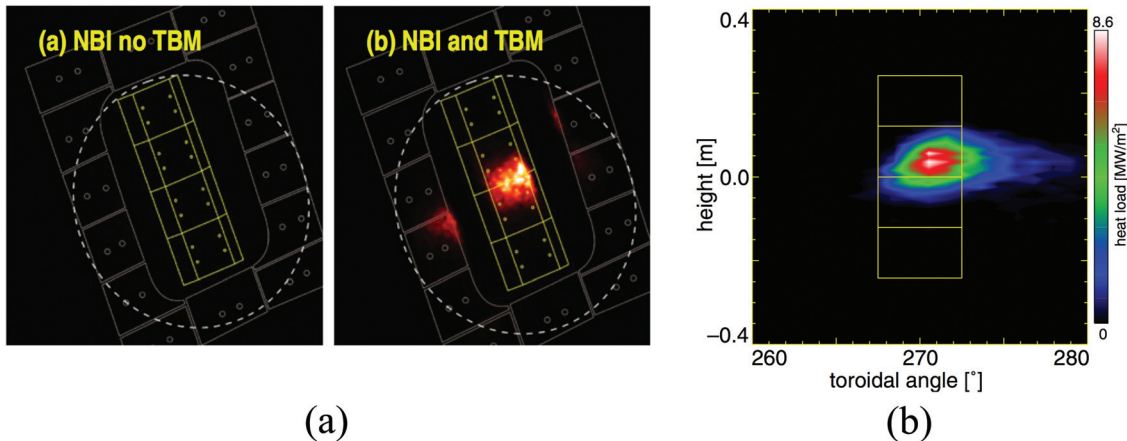


FIG. 11. (a) Infrared measurements of heat flux on DIII-D graphite tiles with TBM simulation coil effects turned off and on, (b) simulation of NBI loss heat flux on tiles from the SPIRAL code. (a) Reprinted with permission from G. J. Kramer, A. McLean, N. Brooks *et al.*, Nucl. Fusion **53**, 123018 (2013). Copyright 2013 IAEA.<sup>187</sup> and (b) reprinted with permission from G. J. Kramer, B. V. Budny, R. Ellis *et al.*, Nucl. Fusion **51**, 103029 (2011). Copyright 2013 IAEA.<sup>188</sup>

studied both for ITER and in DIII-D, where a toroidally localized set of coils were used to simulate the effect of test blanket module ripple. For ITER, the field perturbations arise from the fact that test blanket modules will contain significant masses of ferritic steel. Ferritic steel alloys are likely to remain present in future fusion reactors due to their superior properties<sup>101</sup> in high temperature/high radiation environments. A variety of orbit Monte Carlo slowing-down models have been developed and applied to both ITER with TBMs and to DIII-D with TBM simulation coils. These follow a large number of alpha particle (ITER) or beam ion (DIII-D) orbits in the presence of energy and pitch angle scattering. Heat loads are accumulated as orbit trajectories leave the plasma and intersect the wall. An example of modeling the DIII-D TBM coil-induced losses is shown in Figure 11 using the Spiral full Lorentz orbit model.<sup>102</sup> A variety of models have been applied to this case, and show generally good agreement with infrared camera measurements of localized heating in the graphite tiles that are present near the TBM mock-up coil location. Based on this validation, many of the same models<sup>7,90,163</sup> have been applied to the ITER TBM case. An example<sup>163</sup> of localized alpha particle losses for the ITER TBM case is shown in Figure 12. Under quiescent plasma conditions (no instabilities taken into account), the predicted TBM induced heat fluxes of escaping alpha particles incident on the first wall have remained under the prescribed limits (for ITER, this was set at 50 kW/m<sup>2</sup>). Efforts in this type of modeling are continuing as the effect of various plasma instabilities are taken into account and also losses are followed down into the divertor chamber.

In the case of stellarators and RFPs, EP confinement has been extensively evaluated with respect to its impact on heating efficiency, first wall heat loads, and for comparison with fast ion loss diagnostics. For heliotron/torsatron configurations, such as LHD, ATF, and CHS, significant improvements in EP confinement are possible by shifting the plasma inward. This lines up the minimum values of B as one follows a field line, lowers the ripple strength and results in better-centered fast ion orbits; such effects were originally

noted in Ref. 103 using analytical field models and are known as sigma-optimization. This effect was analyzed for the LHD stellarator with the GNET global particle simulation model<sup>104</sup> and indicated about a factor of  $\sim 3$  improvement in trapped fast ion densities as the magnetic axis is shifted in from 3.75 m to 3.53 m. Similar improvements were seen in experimental charge exchange measurements of the

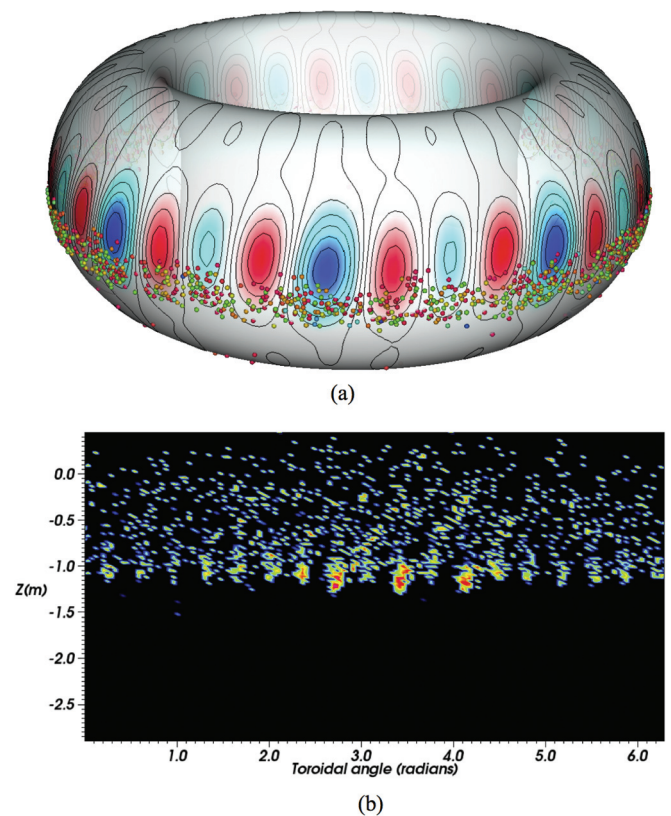


FIG. 12. Alpha particle losses in ITER (a) through last closed flux surface with 3D magnetic field perturbations from TF ripple to TBMs superimposed, and (b) heat flux histogram. (a) and (b) Reprinted with permission from D. A. Spong, Phys. Plasmas **18**, 056109 (2011). Copyright 2011 American Institute of Physics.

fast ion component. In parallel, this form of orbit optimization also applies to the neoclassical transport properties of the thermal plasma. GNET also includes capabilities for simulating RF heating and has been applied to both to ICRF ion tails and ECRF produced suprathermal electron populations. Fast ion and alpha particle losses have been evaluated in a variety of more recent modular coil optimized stellarators. Neutral beam losses were calculated<sup>105</sup> using 5D Monte Carlo methods for the compact NCSX stellarator, indicating 10%-15% energy losses. Alpha particle losses have been evaluated in a number of stellarator reactor designs,<sup>106–108</sup> indicating that with sufficient optimization, very low levels of alpha loss are attainable. Neutral beam losses were evaluated in W7-X<sup>109</sup> and studies made of their sensitivity to plasma  $\beta$  and adjustments of in the main and auxiliary coil currents, indicating that improved beam ion confinement results as the plasma  $\beta$  is raised. Studies of fast ion confinement for LHD in the presence of MHD<sup>110</sup> and Alfvén instabilities<sup>111</sup> have been done using both experimental scintillator-based lost-fast ion probe data (SLIP) and modeling with a guiding center orbit trajectory code (DELTAS5D<sup>163</sup>) that includes fluctuating TAE mode structures with down-chirping frequencies. In both the measurements and modeling, two loss regimes were found: at low TAE amplitudes, the fast ion flux to the wall scaled as  $\delta B_{\theta,TAE}$  (convective), while at higher TAE amplitudes the losses scaled as  $(\delta B_{\theta,TAE})^2$  (diffusive). In the case of RFPs, neutral beam injection has been used on the MST device and studies made of fast ion confinement in both the conventional axisymmetric<sup>112</sup> and the spontaneous single helicity (SHAx) modes<sup>113</sup> of operation. Higher losses of beam ions were observed in the single helicity mode, especially for the hydrogen ions, due to the symmetry-breaking (ripple) effects in the central region of the plasma.

#### D. Neoclassical transport

3D configurations introduce unique neoclassical transport physics characteristics not present in axisymmetric tokamaks. These are a consequence of the uncompensated radial drifts that characterize deeply trapped particles and the large orbit excursions that are present in the trapped-passing region of velocity space. Also, the breaking of axisymmetry requires that ambipolarity ( $\Gamma_{ion} = \Gamma_{electron}$ ) must be explicitly imposed, leading to a nonlinear equation for the radial electric field; in the tokamak ambipolarity is automatically satisfied and the electric field is only explicitly determined if higher order gyro-viscous effects are introduced or if plasma rotation is included.<sup>114</sup>

An example of the different transport regimes in a 3D configuration is shown in Figure 13. This is based on a calculation of the monoenergetic density diffusion coefficient done with the DKES (Drift Kinetic Equation Solver)<sup>115</sup> for the LHD stellarator with a finite level of ambipolar electric field included. The Pfirsch-Schlüter (PS) and plateau regimes are present in both stellarators and tokamaks. The ripple transport (or  $1/\nu$  regime) is unique to 3D systems; this scaling with collision frequency becomes dominant when collisions are sufficiently infrequent that the uncompensated

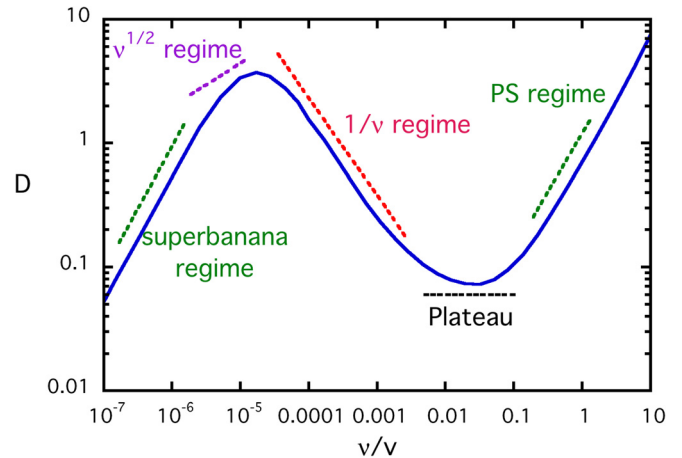
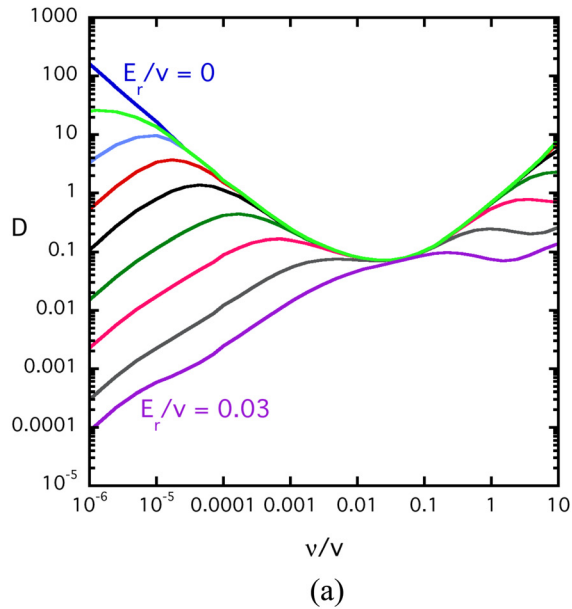


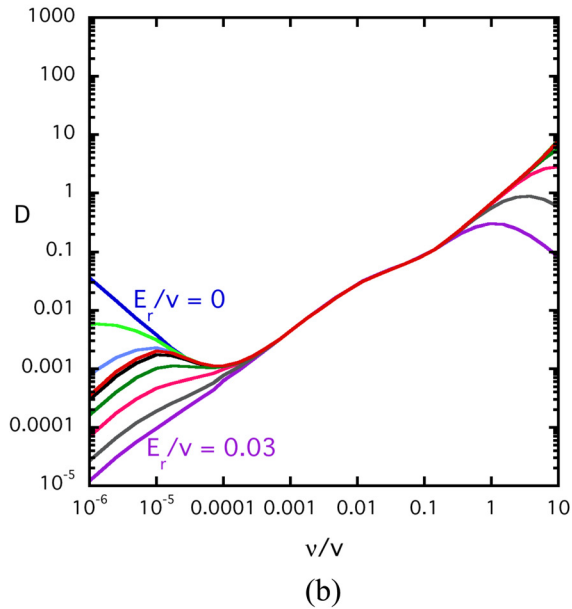
FIG. 13. Stellarator neoclassical transport regimes (monoenergetic density diffusion coefficient is plotted vs. collision frequency/velocity).

radial drifts of the deeply trapped orbits and excursions of transitional orbits are active at transporting them away from flux surface in between collisions. In this regime, increasing collisionality actually improves confinement by limiting the movement of these classes of orbits away from their initial flux surface locations. An analogy can be made to the way in which a large crowd of people in a room can slow down an individual's progress towards an exit door. Next, as collisionality is lowered even further, such orbits experience weak  $E \times B$  and  $B \times \nabla B$  drift components that can compensate the radial drifts, causing their orbits to close poloidally, and leading to the superbanana regime. In this regime, transport scales with collisionality in a more normal way, which can be related to a collision frequency times an effective step size. In between the ripple and superbanana regimes isolated regimes with different collisionality scaling enter in as D transitions smoothly from a  $D \propto 1/\nu$  to a  $D \propto \nu$  scaling. In Figure 14(a), a similar plot is given for the monoenergetic density diffusion coefficient in LHD, showing the dependences on both the collisionality and ambipolar electric field parameters ( $\nu/v, E_r/v$ ). At  $E_r=0$  or small finite  $E_r$ , there is no low  $\nu$  superbanana regime for the collisionalities examined here, only the  $1/\nu$  ripple regime. As  $E_r$  is increased, a superbanana regime enters in, and as it is further increased, the  $1/\nu$  ripple regime eventually disappears. As indicated, for this case, and for most stellarators, there is a very strong variation with  $E_r$  at low collisionalities. In Figure 14(b), the same calculation is done for a tokamak (DIII-D in this case) with ELM coil 3D perturbed fields included. As can be seen, the stellarator-like dependence of D on electric field only appears at low collisionalities, well below the plateau regime. Also, the general level of the diffusion coefficient is lower at equivalent collisionalities than for the stellarator case.

A simple and convenient way to characterize low collisionality neoclassical transport across different 3D systems is the effective ripple<sup>116</sup> parameter  $\epsilon_{eff}$ . This provides a single quantity that contains the configuration dependent part of the  $1/\nu$  asymptotic  $E_r=0$  ripple monoenergetic transport coefficient  $D/D_{plateau} = (4/3\pi)^2(2\epsilon_{eff})^{3/2}/\nu^*$ , where  $D_{plateau}$  is the plateau value of the diffusion coefficient<sup>125</sup> and



(a)



(b)

FIG. 14. Neoclassical monoenergetic density diffusion coefficients vs. collisionality and ambipolar electric for (a) a stellarator (LHD) and (b) a tokamak with 3D effects from ELM control coils.

$\nu^* = R_0 \nu / (\dot{\nu} v)$ , and thus is useful for comparing different configurations. In Figure 15,  $\epsilon_{\text{eff}}^{3/2}$  is plotted for a number of stellarators, several tokamaks with 3D effects, and an RFP single helicity (SHAx) state. As indicated, the earlier stellarators had higher values ( $10^{-3} < \epsilon_{\text{eff}}^{3/2} < 10^{-1}$ ) than the more recent optimized stellarators ( $10^{-4} < \epsilon_{\text{eff}}^{3/2} < 10^{-3}$ ); tokamaks with only TF ripple are quite low, while those with ELM coils are about a factor of 10 below the best optimized stellarators. The RFP single helicity case is in the range of the un-optimized stellarators near the center of the plasma, but drops to the level of 3D tokamaks near the edge, reflecting the localization of the helical core to the center region, accompanied by a nearly axisymmetric outer region.

As mentioned above, neoclassical transport in 3D configurations is not automatically ambipolar ( $\Gamma_i$ , ion particle flux,  $= \Gamma_e$ , electron particle flux); the balance of  $\Gamma_i$  with  $\Gamma_e$

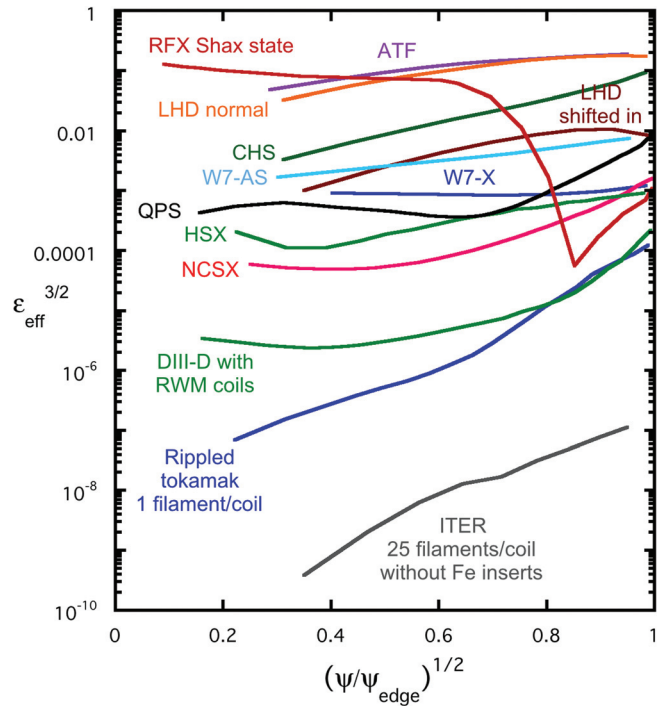


FIG. 15. Effective ripple coefficient vs. normalized toroidal flux for a selection of stellarators, tokamaks with 3D effects, and an RFP single helicity state.

in a 3D system will only occur for particular values of electric field for which  $\sum e_a \Gamma_a = 0$ . Figure 16 shows an example of this phenomenon, taken from a transport analysis<sup>117</sup> of the HSX stellarator. For this case, there are three points where  $\Gamma_i = \Gamma_e$ . The usual naming convention has been to identify the root with inward pointing electric field ( $E_r < 0$ ) as the ion root since it can be related to the ion flux rising to meet the electron flux, while the farthest right hand root ( $E_r > 0$ ) is the electron root since the electron flux is dropping to meet the ion flux. In between there is often a third root that is not stable due to the form of the electric field equation:  $\partial E_r / \partial t \propto \Gamma_e - \Gamma_i$  (this is derived from the radial component of

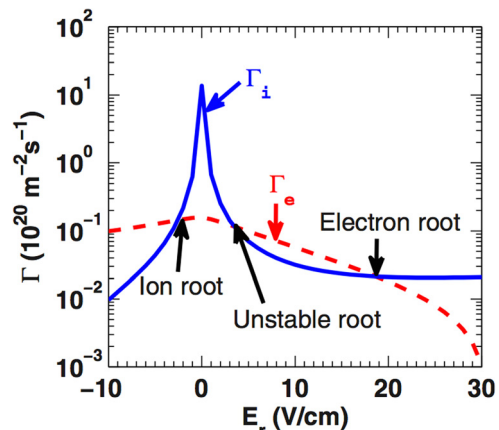


FIG. 16. Ion and electron fluxes vs. electric field for the HSX stellarator. Reprinted with permission from J. Lore, W. Guttenfelder, A. Briesemeister et al., Phys. Plasmas 17, 056101 (2010). Copyright 2010 American Institute of Physics.

Ampere's law). The instability of this third root is related to the fact that if  $E_r$  is perturbed to a larger (smaller) value, then  $\Gamma_i$  decreases (increases) and  $\Gamma_e$  increases (decreases); this further increases (decreases)  $E_r$ , resulting in linear instability. However, for the points identified as ion and electron roots, the responses to  $E_r$  perturbations are in a restoring/stabilizing direction; increasing (decreasing) perturbations in  $E_r$  lead to decreasing (increasing) changes in  $\partial E_r / \partial t$ . Due to the local diffusive approximation of the neoclassical transport model described above, the ambipolarity condition must be solved on each flux surface. There has been interest<sup>118</sup> in scenarios in which the ion root is present over part of the plasma and the electron root in other regions since this would create strong localized electric field shearing that could play a role in transport barrier formation. Methods for driving the ambipolar balance to the electron root have been of interest since the electric field is larger causing the particle and energy fluxes of both species tend to be lower at the electron root than the ion root; also, impurity accumulation has been predicted<sup>119,120</sup> to be less of an issue for the electron root.

The above discussion of neoclassical transport is focused for simplicity on the monoenergetic density transport coefficient  $D_{11}$  that goes with the density gradient. The full neoclassical transport description involves at least a  $3 \times 3$  matrix of coefficients and includes coefficients that go with temperature gradient and electric field terms for both density and heat transport as well as bootstrap current. A number of different models have been developed to obtain these transport coefficients in 3D systems, along with earlier analytic theory;<sup>121</sup> research in this area is ongoing and will be described only in a general way here. As referred to above, the DKES model<sup>115</sup> provides this matrix of coefficients for arbitrary values of collisionality and electric field. This model and other early approaches utilized various approximations to reduce the dimensionality of the kinetic equation. DKES used a radially localized approach, incorporated a pitch-angle scattering collision operator, assumed a distribution function close to Maxwellian and made an incompressible approximation to the  $\mathbf{E} \times \mathbf{B}$  velocity:  $\mathbf{E} \times \mathbf{B}/B^2 \approx \mathbf{E} \times \mathbf{B}/B^2$ . This allowed a variational formulation to be derived in which the energy and radial variable were parameters, providing upper/lower bounds on transport coefficients. The kinetic equation was solved using Fourier expansions in poloidal/toroidal angle and Legendre polynomials in pitch angle. The particle and energy fluxes and the bootstrap current could then be obtained by performing energy integrations over the monoenergetic coefficients. Another approach that was contemporaneous with DKES was the GSRAKE model,<sup>122</sup> which used a ripple-averaged kinetic equation to reduce the dimensionality. GSRAKE required a specific model for the magnetic field, the multi-helicity model<sup>122</sup> to perform the averaging. In addition, particle based Monte Carlo models<sup>123,124</sup> have been developed to obtain local diffusion coefficients, or, in some cases, to test the diffusive transport approximation.<sup>123</sup> These different approaches have been benchmarked for a range of different 3D configurations and covered in detail in Ref. 125.

As mentioned above, the early transport calculations were based on including only a Lorentz pitch-angle

scattering operator. This prevented the conservation of momentum at a microscopic level and precluded accurate prediction of plasma flows and bootstrap currents. While inclusion of a full momentum-conserving collision operator would have made the early methods computationally unwieldy, moments methods were developed<sup>126–129</sup> for correcting this issue at a macroscopic level. This allowed the earlier transport coefficients based on the DKES model to be used and momentum conservation to be achieved at least at a fluid moment level. These approaches were extended to include impurities,<sup>128</sup> higher order energy moment expansions,<sup>129</sup> and incorporated into computational models, such as PENTA.<sup>130</sup> As optimized quasi-symmetric stellarators were developed, interest increased in predictions of plasma flows<sup>131</sup> and bootstrap currents.<sup>132</sup> Plasma flow directions and magnitudes were a distinguishing feature of different optimization approaches and a reliable prediction of bootstrap current is important for stellarator hybrids, which derive significant fractions of their rotational transform from plasma current. Also, stellarators, such as W7-X, with island divertors that require well-defined levels of rotational transform at the plasma edge need accurate evaluations of bootstrap current. More recently, further extensions to stellarator neoclassical theory have been made<sup>133,134</sup> (SFINCS model) that allow 4D models (toroidal/poloidal angles, pitch angle, energy) to be solved directly with momentum-conserving collision operators and full drift trajectories. This has been compared<sup>133</sup> with the DKES model, indicating both regions of agreement and disagreement, depending on the size of the electric field. Another development has been inclusion<sup>135</sup> of poloidal electric field effects, which can be important, especially in the case of impurity transport. Finally, neoclassical transport theory<sup>136,137</sup> specific to the regimes of 3D tokamaks ( $\delta B/B < \rho_{ion}/a$ ) has been derived and used to obtain the neoclassical toroidal viscosity; effects on toroidal viscosity have been of significant interest in tokamak experiments since toroidal flows are readily measured and may influence MHD stability by increasing the probability of locked modes.

### E. Anisotropic transport in regions without nested flux surfaces

As discussed in Sec. IV, there is no guarantee that 3D equilibria will have nested closed flux surfaces. In particular, there are areas near the edge of the plasma and in the divertor scrape-off region that are of significant interest for modeling, but in which the magnetic field lines are chaotic and large magnetic islands are present. When this is coupled with the highly anisotropic heat conductivities ( $\chi_{||}/\chi_{\perp}$  may exceed  $10^{10}$ ) that characterizes fusion systems, an entirely new transport regime must be addressed. In these regimes, the normal cross-field transport that is addressed by neoclassical transport becomes largely irrelevant and transport is dominated by parallel conduction along the wandering field lines. Since these fields are non-integrable, it is impossible to construct discrete coordinate meshes that are well-aligned with the magnetic field structures. Also, attempts to solve such highly anisotropic transport equations using finite differences

or finite element methods experience numerical pollution and eventually are limited by an accumulation of errors. These facts generally force such approaches to use lower values of  $\chi_{\parallel}/\chi_{\perp}$  than are realistic. A new paradigm, the Lagrangian Green's (LG) function method,<sup>138</sup> has been developed to address these challenges. This involves transforming the parallel heat equation into a non-local closure using a Green's function solution. In this form, the standard diffusive transport model can be solved efficiently and accurately even for fields with complex filamentation and braiding;<sup>139</sup> the technique can also be readily generalized to other fractional diffusion models. Applications have been made to heat pulse propagation<sup>140</sup> in chaotic fields, and non-diffusive transport characteristics analyzed. It has been shown that partial transport barriers are possible even with chaotic magnetic fields.

## VI. STABILITY ISSUES FOR 3D CONFIGURATIONS

3D configurations share many of the same stability issues (pressure/current driven MHD, microturbulence, energetic particle instabilities) as axisymmetric systems. However, they also provide unique phenomena and challenges of their own and offer new opportunities for control and optimization of stability. In this section, some of the more recent topics of interest are discussed, along with the tools/methods used for stability analysis.

### A. Energetic particle instabilities

Fast ion driven instabilities were first observed<sup>141</sup> in the W7-AS stellarator, driven by neutral beam injection. This was also the first use of ECE (Electron cyclotron emission) Imaging to diagnose the 2D mode structure of these instabilities. They were dominated by  $(m, n) = (3, 1), (5, 2), (2, 1)$ , and  $(5, 3)$  modes that tracked variations in the  $\dot{\psi}$  profile and followed an Alfvénic frequency scaling [ $\omega \propto 1/(m_{ion} n_{ion})^{1/2}$ ] as the plasma ion mass density was varied. Since then there have been many observations of both fast ion and suprathermal electron driven Alfvén modes in different stellarators, including CHS,<sup>142</sup> LHD,<sup>143</sup> TJ-II,<sup>144,154</sup> H-1N,<sup>145</sup> Heliotron-J,<sup>146</sup> and HSX.<sup>147</sup> In addition, Alfvénic modes have been observed in reversed field pinches,<sup>148</sup> both in the normal operational mode and in single helicity 3D states. As with tokamaks, interest in these instabilities is motivated by concerns about damage to plasma-facing components in reactors, loss of heating efficiency, and diagnostic use (e.g., inferring properties of the  $\dot{\psi}$  profile and dynamical changes in the ion density).

In similarity with Alfvén instabilities in axisymmetric systems, the analysis of these instabilities begins with calculations of the Alfvén gap structure,<sup>149</sup> identification of eigenmodes with a global structure<sup>150,151</sup> within open gaps, perturbative stability analyses, and, more recently, development of hybrid fluid-kinetic and gyrokinetic models. The modes can be classified into several categories: modes in continuum gaps produced by poloidal couplings (TAE, EAE), modes in continuum gaps produced by helical and toroidal mode couplings (HAE, MAE), extremal modes that occur above or below a continuum minimum/maximum

(GAE, RSAE), and beta-induced and acoustic coupled modes (BAE, BAAE). The naming conventions arise from the type of mode interaction responsible for the Alfvén spectral gap within which the mode resides. The “AE” stands for Alfvén Eigenmode and the prefixes T = toroidal, E = elliptical, H = helical, M = mirror, B = beta, BA = beta acoustic. The modes created by helical/toroidal mode couplings (HAE, MAE) are unique to 3D configurations and are present due to the toroidal variations in the equilibrium magnetic field.

This leads into the topic of mode families,<sup>152,157</sup> which is basic to all aspects of macroscopic stability analysis of 3D systems. For the axisymmetric tokamak, the toroidal mode number may be considered a good quantum number since the equilibrium fields include only  $n = 0$  and provide no coupling between instabilities having different  $n$  values. Linear instabilities at arbitrary values of  $n$  may then be considered independently; they will only couple with each other nonlinearly. In the case of 3D systems, the equilibrium has a field-period periodicity (as described in Sec. II), i.e., it will include not only  $n = 0$ , but also  $n = \pm N_{fp}, \pm 2N_{fp}, \pm 3N_{fp}, \dots$ . This fact implies that the toroidal mode number is no longer a good quantum number, but groups of  $n$ 's known as mode families must be considered together. The coupling rules are that for a mode family centered on  $n$ , a sequence of other toroidal modes, denoted by  $n'$  also need to be included, where  $n' \pm n = kN_{fp}$ , with  $k = 0, 1, 2, \dots$ . As a result of this coupling, a sequence of  $n$ 's will need to be included even for linear stability analysis of 3D systems (up to some truncation point); however, there will only be a finite set of mode families to consider since they repeat themselves beyond a certain point. For even values of  $N_{fp}$ , there are  $I + N_{fp}/2$  mode families and for odd values of  $N_{fp}$ , there are  $(N_{fp} - 1)/2 + I$  mode families. In Figure 17, the toroidal mode numbers contained in the  $n = \pm I$  mode family, and the number of different mode families are plotted for devices with different numbers of field periods. Typically, the toroidal mode couplings are less dominant for devices with high field periods, due to the large jumps in  $n$ , than for low field period systems. In modeling lower field period configurations, the analysis also becomes more demanding as toroidal mode couplings become more closely spaced and more  $n$ 's must be included.

Several examples of Alfvén modes in stellarators are given in Figure 18. Figures 18(a)–18(c) present the 3D coupled continuum and RSAE mode structure from an LHD case that had a weakly reversed shear region<sup>153</sup> in the  $\dot{\psi}$  profile near the axis; such a profile was created using off-axis neutral beam current drive. This was an  $n = 1$  dominated mode that had very weak coupling to adjacent  $n$ 's, as is expected for a high field period device ( $N_{fp} = 10$ ). Figures 18(d)–18(f) present the 3D coupled continuum from the lower field period ( $N_{fp} = 4$ ) TJ-II device<sup>154</sup> and an edge-localized HAE mode structure. For this mode and the other gaps indicated, more significant toroidal coupling was present due to the lower field periods and lower aspect ratio of TJ-II.

The stability analysis of energetic particle instabilities in 3D equilibria has progressed from semi-analytical models,<sup>155</sup> to perturbative approaches, hybrid particle-MHD, and

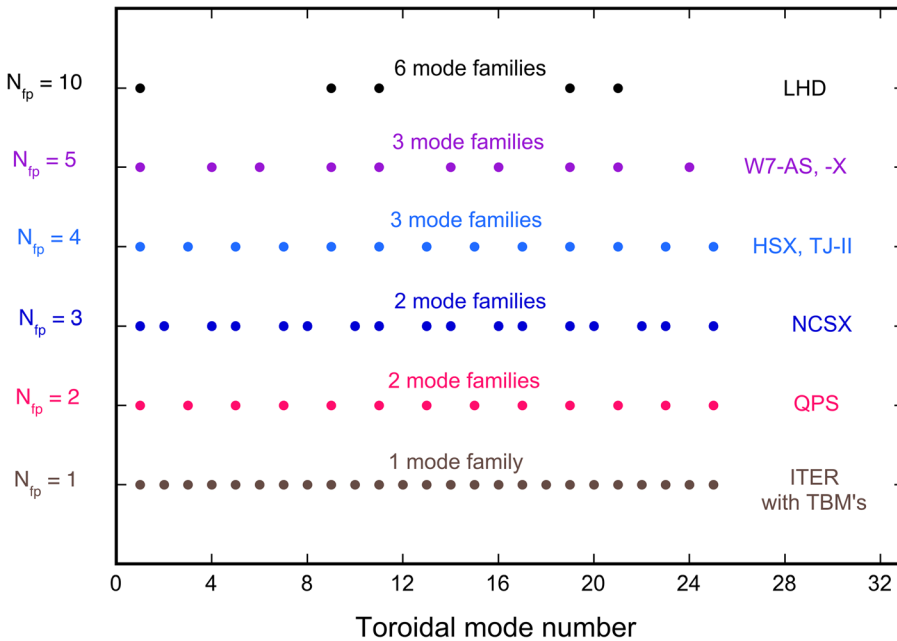


FIG. 17. Toroidal mode couplings for the  $n = \pm 1$  mode family as a function of field periods.

gyrokinetic models. The first perturbative approach was the CAS3D-K model,<sup>156</sup> which utilized stable Alfvén gap eigenfunctions from the CAS3D MHD  $\delta W$  code<sup>157</sup> and solved the linearized fast, thermal ion and electron kinetic equations for growth and damping rates, keeping the mode structure and real frequency fixed. A next step in the development of perturbative models (i.e., fixed MHD mode structure and real frequency) was to include finite orbit width effects using  $\delta f$  methods that evaluate wave-particle energy transfer rates. By following a large number of fast ion orbits in the presence of

the AE mode of interest, and accumulating averages of energy transfer rates, growth rates could be inferred. This approach has been incorporated in codes such as AE3D-K,<sup>158</sup> Venus,<sup>159</sup> and EUTERPE.<sup>160</sup> The hybrid approach is to couple a particle  $\delta f$  kinetic equation solution to an MHD model, and this is used in the MEGA<sup>161</sup> code, which has been applied to LHD. Finally, several global gyrokinetic PIC codes are under development for 3D systems (GTC<sup>162</sup> and EUTERPE<sup>160</sup>).

The study of energetic particle driven instabilities in 3D tokamaks is at an earlier stage of development than for

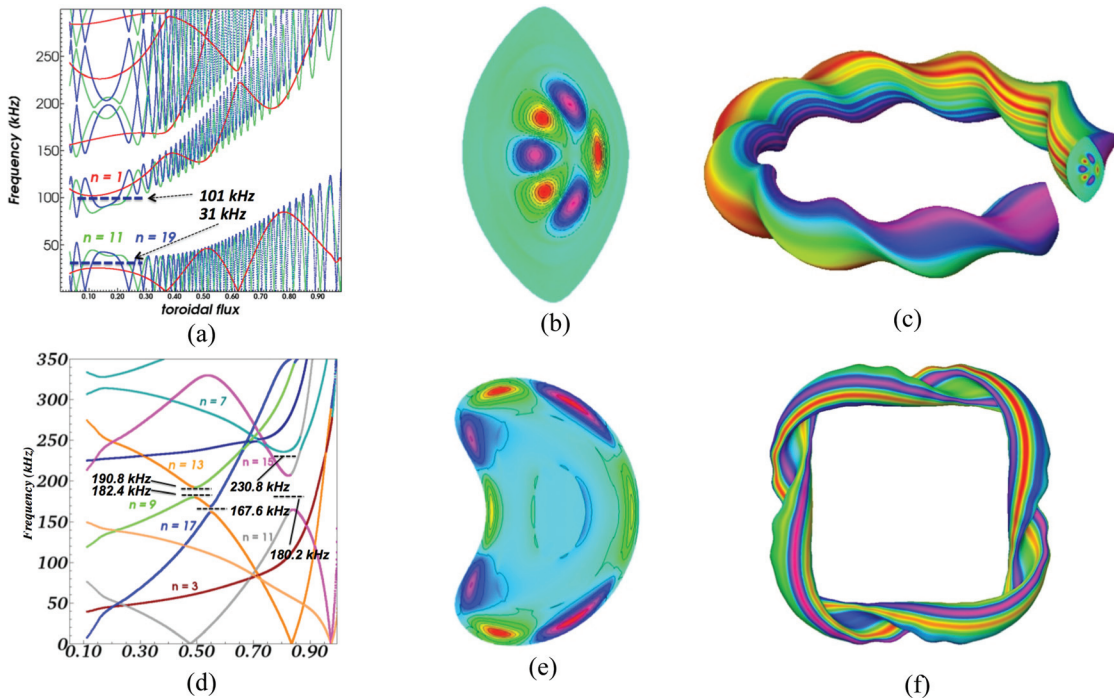


FIG. 18. (a) Alfvén continuum for LHD reversed shear case, (b) 2D mode structure of 31 kHz mode, (c) 3D mode structure of 31 kHz mode, (d) Alfvén continuum for TJ-II case, (e) 2D mode structure of 230.8 kHz mode, and (f) 3D mode structure of 230.8 kHz mode. (a)–(c) Reprinted with permission from K. Toi, AIP Conf. Proc. **1478**, 116-128 (2012). Copyright 2012 American Institute of Physics.<sup>189</sup> (d)–(f) Reprinted with permission from A. V. Melnikov, L. G. Eliseev, E. Ascasibar *et al.*, Nucl. Fusion **52**(12), 123004 (2012). Copyright 2012 IAEA.

stellarators. High-resolution continuum studies<sup>163</sup> have demonstrated the fine scale TF ripple-produced gap structures that are present as high  $n$  AE modes couple with ripple with similar wavelengths. Experiments on NSTX<sup>164</sup> have recently studied both enhanced losses of energetic particle populations with 3D ELM control fields present and regimes where fast ion confinement is not strongly influenced, but AE stability may be suppressed by enhanced continuum damping from the toroidal mode couplings introduced by the 3D coils. Figure 19 displays the Alfvén continuum changes that have been predicted with and without 3D effects from the STELLGAP code<sup>149</sup> for the  $n = 2$  Alfvén mode. Suppression of the  $n = 2$  mode was observed on NSTX with activation of the ELM coils in a regime, where fast ion confinement was not strongly affected.<sup>165</sup> As indicated in Figure 19(b), the 3 field period 3D equilibrium couplings of the  $n = 2, 5, \text{ and } 8$  modes near the edge create a localized modification in the continuum structure, which could increase continuum damping in the frequency range (red line) where the  $n = 2$  instability was observed.

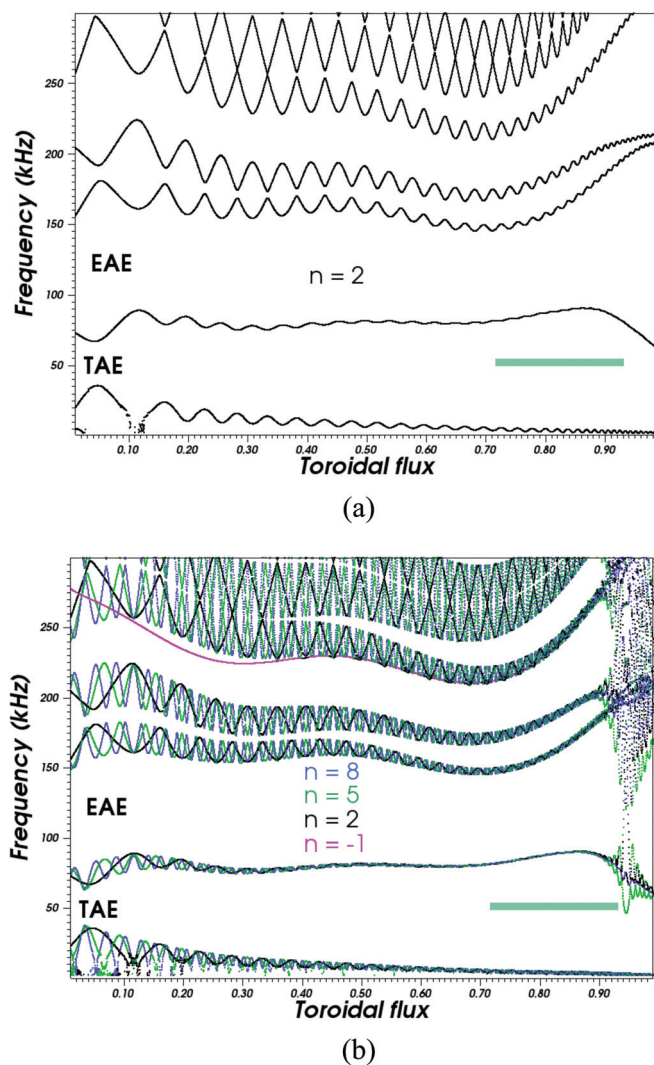


FIG. 19. (a)  $n = 2$  Alfvén continua for axisymmetric NSTX with observed mode frequency indicated in green; (b)  $n = 2$  mode family (coupled to  $n = -1, 5, \text{ and } 8$ ) for NSTX with 3 field period ELM coil effects.

## B. Micro-turbulence

In similarity with tokamaks, 3D configurations experience plasma transport from microturbulence and this generally dominates the transport physics. Confinement scaling databases have been accumulated for stellarators and scaling laws inferred<sup>166,167</sup> that are similar to tokamak gyro-Bohm scalings with an H-mode enhancement factor; a configuration scaling function, based on neoclassical effects, has also been identified.<sup>166</sup> Both linear<sup>168</sup> and nonlinear simulations<sup>169</sup> of core microturbulence candidate modes, such as the ITG (Ion Temperature Gradient) and TEM (Trapped Electron Mode) instabilities have been made for a variety of stellarators. Recently, the possibility of optimizing stellarators to reduce turbulent transport has been explored. A variety of proxy target functions have been investigated,<sup>170</sup> including linear growth rate estimates, quasilinear/mixing length estimates of the heat flux, and direct linear calculations of growth rates from the GENE model. Applications have been made to NCSX, W7-X, and HSX. A recent optimization, based on using the flux-surface version of GENE has resulted in a turbulence optimized stellarator configuration<sup>171</sup> that was evolved from W7-X as a starting point. The differential evolution option<sup>172</sup> of STELLOPT was used. The optimization history, demonstrating a significant improvement in the ITG target function, is shown in Figure 20(a) and the resulting improvement in the post-evaluated ion heat flux is shown in Figure 20(b) between the initial W7-X shape and the optimized MPX configuration. The possibility of optimizing stellarators for reduced levels of microturbulence transport is an exciting new direction for configuration design.

## C. Instabilities in the 3D tokamak edge

The tokamak edge pedestal and scrape-off layer are important, but challenging regions for 3D modeling. Axisymmetric models, such as the ELITE<sup>173</sup> model, have been developed that successfully predict characteristics of plasma gradients in the pedestal region, and the ELM instabilities they drive by balancing off the marginal stability boundaries for peeling and ballooning instabilities. Here, peeling instabilities are global external current gradient-driven instabilities, while ballooning instabilities are localized pressure gradient driven modes. The edge is also the region that is most likely to be modified by the 3D magnetic field perturbations from ELM coils. These will, at low levels, introduce corrugations in flux surfaces [recall Figure 7(a)], and at higher levels, produce islands and chaotic field lines. To the extent that corrugations are resonant with the field line helicity, they can also facilitate unstable external kink modes. Work on this area of 3D physics is still at an early phase, due to the difficulties associated with resolving regions with high shear, many coupled modes/resonances, and the low field period characteristics of the 3D equilibria. Two recent approaches are the direct application<sup>174</sup> of global  $\delta W$  MHD stability analysis and the development of coupled high- $n$  (ballooning) and intermediate- $n$  (peeling) models that include 3D fields.<sup>175</sup> In Ref. 174, the CAS3D model was applied to low  $n$  ( $\leq 4$ ) modes for several cases: a tokamak

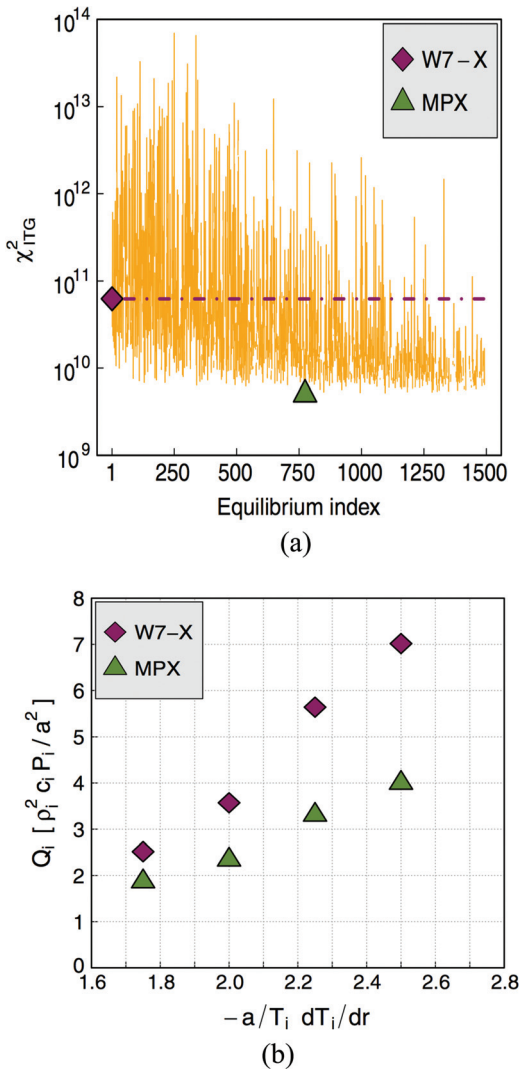


FIG. 20. (a) STELLOPT minimization of ITG target function using differential evolution algorithm; (b) Ion heat flux comparison from GENE simulation. Reprinted with permission from P. Xanthopoulos, H. E. Mynick, P. Helander, Y. Turkin, G. G. Plunk, F. Jenko, T. Göürler, D. Told, T. Bird, and J. H. E. Proll, Phys. Rev. Lett. **113**, 155001 (2014). Copyright 2014 American Institute of Physics.

with a helical core; RMP coils in ASDEX upgrade; and ITER with TBMs. Both stabilizing and destabilizing effects of the ELM coils and TBM effects were seen. In Ref. 175, an analogue of the ELITE peeling-balloonning model was developed for 3D systems by using multiple-scale techniques and energy minimization methods.

#### D. MHD instabilities in stellarators and the optimization of 3D systems

MHD instability analysis for stellarators has predominantly focused on pressure-driven modes, due to the small levels of plasma current that characterize most stellarators. Exceptions to this are the hybrid systems, which augment the vacuum transform with that provided by limited amounts of plasma current; these systems must also take into account current driven modes.<sup>176</sup> The simplest criteria for pressure-driven modes are those obtained in the interchange limit ( $k_{||}/k_{\perp} \ll 1$ ) and include the magnetic well condition

( $V'' < 0$  where  $V' = \text{specific volume} = \oint dl/B$ ) and the Mercier criterion.<sup>177</sup> These lead to conditions local to each flux surface that are readily evaluated from plasma equilibrium quantities. Ballooning stability models, such as COBRA,<sup>178</sup> have also been developed and provide efficient evaluations that can be used in optimizations. Stellarator optimizations have typically targeted at least the magnetic well, Mercier, and ballooning stability conditions. For global linearized MHD, models (CAS3D<sup>157</sup> and Terpsichore<sup>179</sup>) based on the  $\delta W$  variational principle are used; these have been applied both to pressure and current driven instabilities. Finally, several initial value MHD models, such as NORM,<sup>180</sup> FAR3D,<sup>181</sup> and M3D,<sup>176</sup> have been applied both linearly and nonlinearly. A topic of long-standing interest for MHD models is the “soft  $\beta$ -limit” characteristic of stellarators and the fact that experiments seem to routinely exceed stability limits predicted by theory. For example, LHD has achieved<sup>182</sup> peak  $\beta$ 's of 5.1% and W7-AS has achieved<sup>183</sup>  $\sim 7\%$ . This has recently been analyzed<sup>180</sup> for the case of LHD using the NORM nonlinear MHD code and a multi-scale approach that allows the pressure profile to slowly evolve in a self-organized manner uncoupled from the MHD fields. This results in many locally flattened regions in the pressure, but avoids disruptive behavior and achieves higher  $\beta$ 's, albeit lower than those seen in the experiment. For the both experiments, some degree of magnetic well self-stabilization may also have contributed. Magnetic well stabilization and second stability access was a key feature of the ATF stellarator design, and evidence<sup>184</sup> of this was observed as heating power was increased. Second stability for ballooning stability in compact quasi-omnigenous stellarator configurations was reported, leading to hybrid systems with very high  $\beta$  limits<sup>185</sup>—volume averaged ballooning  $\beta$  limits up to 23%. Second stable regimes were also found for QPS configurations.<sup>186</sup> This ability for stellarators to achieve high  $\beta$ 's experimentally without strong disruptions and in optimized designs offers attractive opportunities for reactor designs, given the strong dependence of reactor cost on plasma  $\beta$ .

#### VII. CONCLUSIONS

Symmetry-breaking and 3D physics effects exist to some degree in all toroidal plasma confinement devices and are increasingly used to achieve control and improved plasma performance objectives. Exploration of the 3D design space is one of the major remaining areas of opportunity for the optimization of fusion confinement devices. Specific directions that are currently of interest include: (1) the tokamak 3D edge—optimization for ELM suppression, divertor structures, control of scrape-off layer, and detachment; (2) improved RFP confinement and sustainment through spontaneous helical states; and (3) new directions in stellarator optimization—transport, microturbulence, MHD stability, and energetic particle physics. The increasing availability of computational resources and development of new theoretical methods is well aligned with the needs for improved modeling of 3D physics issues. The significant interest that is now directed toward 3D effects in tokamaks, stellarators, and RFPs also provides excellent opportunities for testing and

validating new simulation models that have been designed with application to all of these systems taken into account. This tutorial paper has presented an overview of a range of 3D physics topics that apply to all toroidal confinement devices. Those interested in greater depth on specific topics are directed to the extended list of references provided and ongoing research that is actively reported on in these areas.

## ACKNOWLEDGMENTS

This material based on work was supported both by the U.S. Department of Energy, Office of Science, under Contract No. DE-AC05-00OR22725 with UT-Battelle, LLC and under the U.S. DOE SciDAC GSEP Center. This tutorial has benefitted from discussions with many colleagues, including: Jeffrey Harris, Andreas Wingen, Alessandro Bortolon, Steve Hirshman, Diego del-Castillo-Negrete, Jeremy Lore, John Canik, Yasushi Todo, Axel Könies, Lee Berry, John Koliner, John Sarff, Harold Weitzner, Allen Boozer, Allan Reiman, Nate Ferraro, Gerrit Kramer, Harry Mynick, Pavlos Xanthopoulos, Matt Landreman, Per Helander, Anthony Cooper, Kazuo Toi, Sam Lazerson, Mike Zarnstorff, and Kouji Shinohara.

This manuscript has been authored by UT-Battelle, LLC under Contract No. DE-AC05-00OR22725 with the U.S. Department of Energy. The United States Government retains and the publisher, by accepting the article for publication, acknowledges that the United States Government retains a non-exclusive, paid-up, irrevocable, world-wide license to publish or reproduce the published form of this manuscript, or allow others to do so, for United States Government purposes. The Department of Energy will provide public access to these results of federally sponsored research in accordance with the DOE Public Access Plan (<http://energy.gov/downloads/doe-public-access-plan>).

<sup>1</sup>D. D. Ryutov and G. V. Stupakov, "Neoclassical transport in ambipolar confinement systems," Sov. J. Plasma Phys. **4**(3), 278–289 (1978).

<sup>2</sup>R. H. Cohen, "Analytic approximation to resonant plateau transport coefficients for tandem mirrors," Nucl. Fusion **19**, 1579 (1979).

<sup>3</sup>I. Katanuma, Y. Kiwamoto, K. Ishii, K. Yatsu, and S. Miyoshi, "Neoclassical resonant-plateau transport in the noncircular equipotential surface of a tandem mirror," Phys. Fluids B **1**, 1459 (1989).

<sup>4</sup>D. A. D'Ippolito and J. P. Freidberg, "Equilibrium and stability of nonaxisymmetric minimum-B mirrors," Phys. Fluids **25**, 1617 (1982).

<sup>5</sup>W. Halchin, J. F. Clarke, S. M. DeCamp, P. H. Edmonds, J. C. Ezell, J. E. Francis, R. E. Hill, G. G. Kelley, S. O. Lewis, J. R. McNally, Jr., M. Murakami, M. Roberts, M. J. Lubin, and J. M. Soures, IEEE Trans. Nucl. Sci. **18**(4), 42–48 (1971).

<sup>6</sup>D. L. Jassby, H. H. Towner, and R. J. Goldston, "Reduced fusion-neutron production in non-axisymmetric tokamak devices," Nucl. Fusion **18**, 825 (1978).

<sup>7</sup>K. Shinohara, T. Kurki-Suonio, D. Spong, O. Asunta, K. Tani, E. Strumberger, S. Briguglio, T. Koskela, G. Vlad, S. Günter, G. Kramer, S. Putvinski, K. Hamamatsu, and ITPA Topical Group on Energetic Particles, "Effects of complex symmetry-breakings on alpha particle power loads on first wall structures and equilibrium in ITER," Nucl. Fusion **51**, 063028 (2011).

<sup>8</sup>L. Spitzer, "The Stellarator Concept," Phys. Fluids **1**(4), 253 (1958).

<sup>9</sup>T. H. Stix, "Highlights in early stellarator research at Princeton," J. Plasma Fusion Res. Ser. **1**, 3–8 (1998).

<sup>10</sup>J. Nührenberg and R. Zille, Phys. Lett. A **129**, 113 (1988).

<sup>11</sup>A. A. Skovoroda and V. D. Shafranov, Plasma Phys. Rep. **21**, 886 (1995).

<sup>12</sup>J. R. Cary and S. G. Shasharina, Phys. Rev. Lett. **78**, 674 (1997).

<sup>13</sup>R. Lorenzini, E. Martines, P. Piovesan, D. Terranova, P. Zanca, M. Zuin, A. Alfieri, D. Bonfiglio, F. Bonomo, A. Canton, S. Cappello, L. Carraro, R. Cavazzana, D. F. Escande, A. Fassina, P. Franz, M. Gobbin, P. Innocente, L. Marrelli, R. Pasqualotto, M. E. Puiatti, M. Spolaore, M. Valisa, N. Vianello, P. Martin, and RFX-mod Team and Collaborators, Nat. Phys. **5**, 570 (2009).

<sup>14</sup>W. F. Bergerson, F. Auriemma, B. E. Chapman, W. X. Ding, P. Zanca, D. L. Brower, P. Innocente, L. Lin, R. Lorenzini, E. Martines, B. Momo, J. S. Sarff, and D. Terranova, "Bifurcation to 3D helical magnetic equilibrium in an axisymmetric toroidal device," Phys. Rev. Lett. **107**, 255001 (2011).

<sup>15</sup>J. S. Sarff, A. F. Almagri, J. K. Anderson, M. Borchardt, D. Carmody, K. Caspary, B. E. Chapman, D. J. D. Hartog, J. Duff, S. Eilerman, A. Falkowski, C. B. Forest, J. A. Goetz, D. J. Holly, J.-H. Kim, J. King, J. Ko, J. Koliner, S. Kumar, J. D. Lee, D. Liu, R. Magee, K. J. McCollam, M. McGarry, V. V. Mirnov, M. D. Nornberg, P. D. Nonn, S. P. Oliva, E. Parke, J. A. Reusch, J. P. Sauppe, A. Seltzman, C. R. Sovinec, H. Stephens, D. Stone, D. Theucks, M. Thomas, J. Triana, P. W. Terry, J. Waksman, W. F. Bergerson, D. L. Brower, W. X. Ding, L. Lin, D. R. Demers, P. Fimognari, J. Titus, F. Auriemma, S. Cappello, P. Franz, P. Innocente, R. Lorenzini, E. Martines, B. Momo, P. Piovesan, M. Puiatti, M. Spolaore, D. Terranova, P. Zanca, V. Belykh, V. I. Davydenko, P. Deichuli, A. A. Ivanov, S. Polosatkin, N. V. Stupishin, D. Spong, D. Craig, R. W. Harvey, M. Cianciosa, and J. D. Hanson, "Overview of results from the MST reversed field pinch experiment," Nucl. Fusion **53**, 104017 (2013).

<sup>16</sup>R. D. Gill, A. W. Edwards, D. Pasini, and A. Weller, "Snake-like density perturbations in JET," Nucl. Fusion **32**(5), 723–735 (1992).

<sup>17</sup>W. A. Cooper, J. P. Graves, and O. Sauter, "JET snake magnetohydrodynamic equilibria," Nucl. Fusion **51**(7), 072002 (2011).

<sup>18</sup>A. H. Boozer, "Use of non-axisymmetric shaping in magnetic fusion," Phys. Plasmas **16**, 058102 (2009).

<sup>19</sup>A. H. Boozer, "Physics of magnetically confined plasmas," Rev. Mod. Phys. **76**(4), 1071–1141 (2004).

<sup>20</sup>P. Helander, C. D. Beidler, T. M. Bird, M. Drevlak, Y. Feng, R. Hatzky, F. Jenko, R. Kleiber, J. H. E. Proll, Y. Turkin, and P. Xanthopoulos, "Stellarator and tokamak plasmas: A comparison," Plasma Phys. Controlled Fusion **54**, 124009 (2012).

<sup>21</sup>A. H. Boozer, "Non-axisymmetric magnetic fields and toroidal plasma confinement," Nucl. Fusion **55**, 25001–1–80 (2015).

<sup>22</sup>A. Iiyoshi *et al.*, "Overview of the large helical device project," Nucl. Fusion **39**, 1245–1256 (1999).

<sup>23</sup>M. J. Schaffer, J. A. Snipes, P. Gohil, P. de Vrie, T. E. Evans, M. E. Fenstermacher, X. Gao, A. M. Garofalo, D. A. Gates, C. M. Greenfield, W. W. Heidbrink, G. J. Kramer, R. J. La Haye, S. Liu, A. Loarte, M. F. F. Nave, T. H. Osborne, N. Oyama, J.-K. Park, N. Ramasubramanian, H. Reimerdes, G. Saibene, A. Salmi, K. Shinohara, D. A. Spong, W. M. Solomon, T. Tala, Y. B. Zhu, J. A. Boedo, V. Chuyanov, E. J. Doyle, M. Jakubowski, H. Jhang, R. M. Nazikian, V. D. Pustovitov, O. Schmitz, R. Srinivasan, T. S. Taylor, M. R. Wade, K.-I. You, L. Zeng, and the DIII-D Team, "ITER test blanket module error field simulation experiments at DIII-D," Nucl. Fusion **51**, 103028 (2011).

<sup>24</sup>R. L. Dewar and S. R. Hudson, "Stellarator symmetry," Physica D **112**, 275–280 (1998).

<sup>25</sup>H. Renner *et al.*, "Initial operation of the Wendelstein 7AS advanced stellarator," Plasma Phys. Controlled Fusion **31**, 1579–1596 (1989).

<sup>26</sup>J. V. Hofmann, J. Baldzuhn, R. Brakel, Y. Feng, S. Fiedler, J. Geiger, P. Grigull, G. Herre, R. Jaenicker, M. Kick, J. Kisslinger, G. Kühner, F.-P. Penningfeld, A. Runow, F. Sardei, U. Stroth, F. Wagner, A. Weller, H. Wobig, W7-AS-Team, and NBI- and ECRH-Groups, "Stellarator optimization studies in W7-AS," Plasma Phys. Controlled Fusion **38**, A193–A211 (1996).

<sup>27</sup>F. S. B. Anderson, A. F. Almagri, D. T. Anderson, P. G. Matthews, J. N. Talmadge, and J. L. Shohet, "The helically symmetric experiment, (HSX) goals, design, and status," Fusion Technol. **27**, 273–277 (1995).

<sup>28</sup>L.-P. Ku and A. H. Boozer, "Stellarator coil design and plasma sensitivity," Phys. Plasmas **17**(12), 122503 (2010).

<sup>29</sup>P. E. Gill, W. Murray, and M. H. Wright, *Practical Optimization* (Academic, London, 1981).

<sup>30</sup>D. E. Goldberg, *Genetic Algorithms in Search, Optimization, and Machine Learning* (Addison-Wesley, Reading, MA, 1989).

<sup>31</sup>R. Storn and K. Price, "Differential evolution," Dr. Dobb's J. **22**, 18 (1997).

- <sup>32</sup>D. A. Spong, S. P. Hirshman, J. C. Whitson, D. B. Batchelor, B. A. Carreras, V. E. Lynch, and J. A. Rome, “J<sup>\*</sup> optimization of small aspect ratio stellarator/tokamak hybrid devices,” *Phys. Plasmas* **5**(5), 1752–1758 (1998).
- <sup>33</sup>P. Merkel, “Solution of stellarator boundary value problems with external currents,” *Nucl. Fusion* **27**(5), 867–871 (1987).
- <sup>34</sup>D. J. Strickler, L. A. Berry, S. P. Hirshman, J. F. Lyon, D. A. Spong, D. E. Williamson, M. C. Zarnstorff, L.-P. Ku, A. Brooks, S. R. Hudson, D. A. Monticello, G. H. Neilson, N. Pomphrey, A. H. Reiman, and A. S. Ware, “Integrated plasma and coil optimization for compact stellarators,” IAEA-CN-94/FT/P2-06, in Proceedings of the 19th IAEA Fusion Energy Conference, Lyon, France, 14–19 October (2002).
- <sup>35</sup>C. Mercier, *Nucl. Fusion* **4**, 213 (1964).
- <sup>36</sup>C. Alejaldre *et al.*, “TJ-II project: A flexible heliac stellarator,” *Fusion Technol.* **17**, 131 (1990).
- <sup>37</sup>A. F. Almagri, D. T. Anderson, F. S. B. Anderson, P. H. Probert, J. L. Shohet, and J. N. Talmadge, “Helically symmetric stellarator (HSX),” *IEEE Trans. Plasma Sci.* **27**(1), 114–115 (1999).
- <sup>38</sup>V. Erckmann, H.-J. Hartfuss, M. Kick, H. Renner, J. Sapper, F. Schauer, E. Speth, F. Wesner, F. Wagner, M. Wanner, A. Weller, and H. Wobig, “W7-X project: Scientific basis and technical realization,” *Proc. Symp. Fusion Eng.* **1**, 40–48 (1998).
- <sup>39</sup>G. J. Hartwell, M. C. ArchMiller, M. Cianciosa, J. D. Hanson, J. Hebert, J. Herfindal, S. F. Knowlton, X. Ma, D. A. Maurer, M. Pandya, and P. Traverso, “Overview of results from the compact toroidal hybrid experiment,” in *Proceedings of the 40th EPS Conference on Plasma Physics*, EPS 2013, Vol. 1, pp. 557–560.
- <sup>40</sup>M. C. Zarnstorff, L. A. Berry, A. Brooks, E. Fredrickson, G.-Y. Fu, S. Hirshman, S. Hudson, L.-P. Ku, E. Lazarus, D. Mikkelsen, D. Monticello, G. H. Neilson, N. Pomphrey, A. Reiman, D. Spong, D. Strickler, A. Boozer, W. A. Cooper, R. Goldston, R. Hatcher, M. Isaev, C. Kessel, J. Lewandowski, J. F. Lyon, P. Merkel, H. Mynick, B. E. Nelson, C. Nuehrenberg, M. Redi, W. Reiersen, P. Rutherford, R. Sanchez, J. Schmidt, and R. B. White, “Physics of the compact advanced stellarator NCSX,” *Plasma Phys. Controlled Fusion* **43**(12A), A237–A249 (2001).
- <sup>41</sup>B. E. Nelson, R. D. Benson, L. A. Berry, A. B. Brooks, M. J. Cole, P. J. Fogarty, P. L. Goranson, P. Heitzenroeder, S. P. Hirshman, G. H. Jones, J. F. Lyon, P. K. Mioduszewski, D. A. Monticello, D. A. Spong, D. J. Strickler, A. S. Ware, and D. E. Williamson, “Design of the quasi-poloidal stellarator experiment (QPS),” *Fusion Eng. Des.* **66–68**, 205–210 (2003).
- <sup>42</sup>P. E. Moroz, “Stellarator-tokamak hybrid with inclined coils,” *Fusion Technol.* **30**(1), 40–49 (1996).
- <sup>43</sup>P. E. Moroz, “Low-aspect-ratio stellarators with planar coils,” *Plasma Phys. Controlled Fusion* **39**(11), 1841–1859 (1997).
- <sup>44</sup>J. W. Berkery, T. S. Pedersen, J. P. Kremer, Q. R. Marksteiner, R. G. Lefrancois, M. S. Hahn, and P. W. Brenner, “Confinement of pure electron plasmas in the Columbia non-neutral torus,” *Phys. Plasmas* **14**(6), 062503 (2007).
- <sup>45</sup>A. W. Clark, M. Doumet, K. C. Hammond, Y. Kornbluth, D. A. Spong, R. Sweeney, and F. A. Volpe, “Proto-CIRCUS tilted-coil tokamak–torsatron hybrid: Design and construction,” *Fusion Eng. Des.* **89**(11), 2732–2737 (2014).
- <sup>46</sup>D. Spong, J. Harris, W. Reiersen, A. Clark, A. Neilsen, F. Volpe *et al.*, “Recent optimized stellarator designs,” Workshop on Exploratory Topics in Plasma and Fusion Research (EPR2013), 12–15 February 2013, Fort Worth, Texas, (<http://www.iccworkshops.org/epr2013/proceedings.php>).
- <sup>47</sup>M. D. Kruskal and R. M. Kulsrud, “Equilibrium of a magnetically confined plasma in a toroid,” *Phys. Fluids* **1**, 265 (1958).
- <sup>48</sup>H. Grad, *Phys. Fluids* **10**, 137 (1967).
- <sup>49</sup>D. Lortz, *Z. Angew. Math. Phys.* **21**, 196 (1970).
- <sup>50</sup>H. Weitzner, “Ideal magnetohydrodynamic equilibrium in a non-symmetric topological torus,” *Phys. Plasmas* **21**, 022515 (2014).
- <sup>51</sup>S. P. Hirshman and J. C. Whitson, *Phys. Fluids* **26**, 3553 (1983).
- <sup>52</sup>S. P. Hirshman, W. I. van Rij, and P. Merkel, *Comput. Phys. Commun.* **43**, 143 (1986).
- <sup>53</sup>A. Weller, C. Görner, and D. Gonda, “X-ray diagnostics on WENDELSTEIN 7-AS,” *Rev. Sci. Instrum.* **70**, 484 (1999).
- <sup>54</sup>W. A. Cooper *et al.*, *Comput. Phys. Commun.* **180**, 1524–1533 (2009).
- <sup>55</sup>W. A. Cooper, S. P. Hirshman, I. T. Chapman, D. Brunetti, J. M. Faustin, J. P. Graves, D. Pfefferlé, M. Raghunathan, O. Sauter, T. M. Tran, and N. Aiba, “An approximate single fluid 3-dimensional magnetohydrodynamic equilibrium model with toroidal flow,” *Plasma Phys. Controlled Fusion* **56**, 094004 (2014).
- <sup>56</sup>J. D. Hanson, S. P. Hirshman, S. F. Knowlton, L. L. Lao, E. A. Lazarus, and J. M. Shields, “V3FIT: A code for three-dimensional equilibrium reconstruction,” *Nucl. Fusion* **49**(7), 075031–12 (2009).
- <sup>57</sup>S. A. Lazerson, “Three-dimensional equilibrium reconstruction on the DIII-D device,” *Nucl. Fusion* **55**(2), 023009 (2015).
- <sup>58</sup>A. H. Reiman and H. S. Greenside, *Comput. Phys. Commun.* **43**, 157 (1986).
- <sup>59</sup>Y. Suzuki, N. Nakajima, K. Watanabe, Y. Nakamura, and T. Hayashi, “Development and application of HINT2 to helical system plasmas,” *Nucl. Fusion* **46**(11), L19–L24 (2006).
- <sup>60</sup>S. R. Hudson and N. Nakajima, “Pressure, chaotic magnetic fields, and magnetohydrodynamic equilibria,” *Phys. Plasmas* **17**, 052511 (2010).
- <sup>61</sup>S. P. Hirshman, R. Sanchez, and C. R. Cook, “SIESTA: A scalable iterative equilibrium solver for toroidal applications,” *Phys. Plasmas* **18**(6), 062504 (2011).
- <sup>62</sup>N. M. Ferraro, S. C. Jardin, and P. B. Snyder, *Phys. Plasmas* **17**, 102508 (2010).
- <sup>63</sup>Y. Q. Liu, A. Bondeson, C. M. Fransson, B. Lennartson, and C. Breitholtz, *Phys. Plasmas* **7**, 3681 (2000).
- <sup>64</sup>J.-K. Park, A. H. Boozer, and A. H. Glasser, *Phys. Plasmas* **14**, 052110 (2007).
- <sup>65</sup>A. H. Boozer, “Plasma torque and nonambipolar transport,” *Phys. Plasmas* **16**, 052505 (2009).
- <sup>66</sup>A. J. Cole and R. Fitzpatrick, *Phys. Plasmas* **13**, 032503 (2006).
- <sup>67</sup>A. D. Turnbull, N. M. Ferraro, V. A. Izzo, E. A. Lazarus, J.-K. Park, W. A. Cooper, S. P. Hirshman, L. L. Lao, M. J. Lanctot, S. Lazerson, Y. Q. Liu, A. Reiman, and F. Turco, “Comparisons of linear and nonlinear plasma response models for non-axisymmetric perturbations,” *Phys. Plasmas* **20**, 056114 (2013).
- <sup>68</sup>A. Reiman, A. Turnbull, T. E. Evans, E. Lazarus, J. Breslau, J. Canik, A. Cerfon, C.-S. Chang, N. M. Ferraro, R. Hager, J. King, M. Lanctot, S. Lazerson, Y. Liu, G. McFadden, D. Monticello, J.-K. Park, C. Sovinec, Y. Suzuki, F. Turco, and P. Zhu, “A cross-benchmarking and validation initiative for tokamak 3D equilibrium calculations,” in *Proceedings of the Twenty-Fifth Fusion Energy Conference (FEC 2014)*, 13–18 October 2014, Saint Petersburg, Russia, IAEA, Vienna, TH/P4-7, Vol. 1.
- <sup>69</sup>P. R. Garabedian, “Three-dimensional analysis of tokamaks and stellarators,” *Proc. Natl. Acad. Sci. U.S.A.* **105**(37), 13716–13719 (2008).
- <sup>70</sup>J. D. King, “Experimental tests of linear and nonlinear 3D equilibrium models in DIII-D,” Abstract ID: BAPS.2014.DPP.TI1.4, Bulletin of the American Physical Society, Invited talk, in *Proceedings of the 56th Annual Meeting of the APS Division of Plasma Physics*, 2015, Vol. 59, p. 15.
- <sup>71</sup>T. E. Evans, M. E. Fenstermacher, R. A. Moyer, T. H. Osborne, J. G. Watkins, P. Gohil, I. Joseph, M. J. Schaffer, L. R. Baylor, M. Becoulet, J. A. Boedo, K. H. Burrell, J. S. deGrassie, K. H. Finken, T. Jernigan, M. W. Jakubowski, C. J. Lasnier, M. Lehnert, A. W. Leonard, J. Lonnroth, E. Nardon, V. Parail, O. Schmitz, B. Unterberg, and W. P. West, “RMP ELM suppression in DIII-D plasmas with ITER similar shapes and collisionalities,” *Nucl. Fusion* **48**(2), 024002–1–10 (2008).
- <sup>72</sup>W. Suttrop, T. Eich, J. C. Fuchs, S. Günter, A. Janizer, A. Herrmann, A. Kallenbach, P. T. Lang, T. Lunt, M. Maraschek, R. M. McDermott, A. Mlynek, T. Pütterich, M. Rott, T. Vierle, E. Wolfrum, Q. Yu, I. Zammuto, and H. Zohm, “First observation of edge localized modes mitigation with resonant and non-resonant magnetic perturbations in ASDEX upgrade,” *Phys. Rev. Lett.* **106**, 225004 (2011).
- <sup>73</sup>J. M. Canik, S. P. Hirshman, R. Sanchez, R. Maingi, J.-W. Ahn, R. E. Bell, A. Diallo, S. P. Gerhardt, B. P. LeBlanc, J. E. Menard, J.-K. Park, M. Podesta, and S. A. Sabbagh, “First use of three-dimensional equilibrium, stability and transport calculations for interpretation of ELM triggering with magnetic perturbations in NSTX,” *Nucl. Fusion* **52**, 054004 (2012).
- <sup>74</sup>J. D. Lore, J. M. Canik, J.-W. Ahn, A. Bortolon, E. D. Fredrickson, M. A. Jaworski, G. J. Kramer, R. Maingi, A. G. McLean, F. Scotti, V. A. Soukhanovskii, and K. Tritz, “Effect of n = 3 perturbation field amplitudes below the ELM triggering threshold on edge and SOL transport in NSTX,” *J. Nucl. Mater.* **438**, S388–S392 (2013).
- <sup>75</sup>T. E. Evans, R. K. W. Roeder, J. A. Carter, and B. I. Rapoport, “Homoclinic tangles, bifurcations, and edge stochasticity in diverted tokamaks,” *Contrib. Plasma Phys.* **44**(1–3), 235–240 (2004).
- <sup>76</sup>T. E. Evans, R. K. W. Roeder, J. A. Carter, B. I. Rapoport, M. E. Fenstermacher, and C. J. Lasnier, “Experimental signatures of homoclinic

- tangles in poloidally diverted tokamaks," *J. Phys.: Conf. Ser.* **7**(1), 174–190 (2005).
- <sup>77</sup>R. K. W. Roeder, B. I. Rapoport, and T. E. Evans, "Explicit calculations of homoclinic tangles in tokamaks," *Phys. Plasmas* **10**(9), 3796–3799 (2003).
- <sup>78</sup>A. Punjabi and A. Boozer, "Homoclinic tangle in tokamak divertors," *Phys. Lett. A* **378**, 2410–2416 (2014).
- <sup>79</sup>R. J. Goldston, "Scrape-off layer flows with pressure gradient scale length  $\sim \text{Rho}_p$ ," *J. Nucl. Mater.* **438**, S372–S374 (2013).
- <sup>80</sup>M. W. Shafer, E. A. Unterberg, D. M. Orlov, T. E. Evans, J. H. Harris, D. L. Hillis, R. Maingi, R. A. Moyer, R. Nazikian, and A. Wingen, "Experimental imaging of separatrix splitting on DIII-D," *Nucl. Fusion* **52**, 122001 (2012).
- <sup>81</sup>N. M. Ferraro, T. E. Evans, L. L. Lao, R. A. Moyer, R. Nazikian, D. M. Orlov, M. W. Shafer, E. A. Unterberg, M. R. Wade, and A. Wingen, "Role of plasma response in displacements of the tokamak edge due to applied non-axisymmetric fields," *Nucl. Fusion* **53**, 073042 (2013).
- <sup>82</sup>D. A. Spong, S. P. Hirshman, and J. C. Whitson, *Plasma Phys. Rep.* **23**, 483 (1999).
- <sup>83</sup>J. A. Rome, "Orbit topology in conventional stellarators in the presence of electric fields," *Nucl. Fusion* **35**, 195 (1995).
- <sup>84</sup>J. R. Cary, C. L. Hedrick, and J. Tolliver, *Phys. Fluids* **31**, 1586 (1988).
- <sup>85</sup>A. H. Boozer, *Phys. Fluids* **27**, 2441 (1984).
- <sup>86</sup>R. B. White, "Canonical Hamiltonian guiding center variables," *Phys. Fluids B* **2**, 845 (1990).
- <sup>87</sup>X. Bonnin, A. Mutzke, C. Nührenberg, J. Nührenberg, and R. Schneider, "Calculation of magnetic coordinates for stellarator fields including islands and the Scrape-off layer," *Nucl. Fusion* **45**, 22–29 (2005).
- <sup>88</sup>R. G. Littlejohn, "Hamiltonian formulation of guiding center motion," *Phys. Fluids* **24**, 1730 (1981).
- <sup>89</sup>J. A. Reusch, J. K. Anderson, and Y. Tsidulko, "Full particle orbit tracing with the RIO code in the presence of broad-spectrum MHD activity in a reversed-field pinch," *Nucl. Fusion* **54**, 104007 (2014).
- <sup>90</sup>T. Kurki-Suonio, O. Asunta, E. Hirvijoki, T. Koskela, A. Snicker, T. Hauff, F. Jenko, E. Poli, and S. Sipilä, "Fast ion power loads on ITER first wall structures in the presence of NTMs and microturbulence," *Nucl. Fusion* **51**, 083041 (2011).
- <sup>91</sup>A. H. Boozer and G. Kuo-Petraovic, "Monte Carlo evaluation of transport coefficients," *Phys. Fluids* **24**, 851 (1981).
- <sup>92</sup>R. J. Goldston, R. B. White, and A. H. Boozer, "Confinement of high-energy trapped particles in tokamaks," *Phys. Rev. Lett.* **47**, 647 (1981).
- <sup>93</sup>L. S. Hall and B. McNamara, "Three-dimensional equilibrium of the anisotropic, finite-pressure guiding-center plasma: Theory of the magnetic plasma," *Phys. Fluids* **18**, 552 (1975).
- <sup>94</sup>M. Landreman and P. J. Catto, "Omnigenity as generalized quasisymmetry," *Phys. Plasmas* **19**, 056103 (2012).
- <sup>95</sup>J. R. Cary and S. G. Shasharina, *Phys. Plasmas* **4**, 3323 (1997).
- <sup>96</sup>P. Helander and A. N. Simakov, *Phys. Rev. Lett.* **101**, 145003 (2008).
- <sup>97</sup>N. Simakov and P. Helander, *Plasma Phys. Controlled Fusion* **53**, 024005 (2011).
- <sup>98</sup>A. H. Boozer, "Transport and isomorphic equilibria," *Phys. Fluids* **26**(2), 496–499 (1983).
- <sup>99</sup>D. A. Garren and A. H. Boozer, *Phys. Fluids B* **3**, 2822 (1991).
- <sup>100</sup>D. A. Spong and J. H. Harris, *Plasma Fusion Res.* **5**, S2039 (2010).
- <sup>101</sup>S. J. Zinkle, J. P. Blanchard, R. W. Callis, C. E. Kessel, R. J. Kurtz, P. J. Lee, K. A. McCarthy, N. B. Morley, F. Najmabadi, R. E. Nygren, G. R. Tynan, D. G. Whyte, R. S. Willms, and B. D. Wirth, "Fusion materials science and technology research opportunities now and during the ITER era," *Fusion Eng. Des.* **89**(7–8), 1579–1585 (2014).
- <sup>102</sup>G. J. Kramer, R. V. Budny, A. Bortolon, E. D. Fredrickson, G. Y. Fu, W. W. Heidbrink, R. Nazikian, E. Valeo, and M. A. Van Zeeland, "A description of the full-particle-orbit-following SPIRAL code for simulating fast-ion experiments in tokamaks," *Plasma Phys. Controlled Fusion* **55**, 025013 (2013).
- <sup>103</sup>H. E. Mynick, T. K. Chu, and A. H. Boozer, "Class of model stellarator fields with enhanced confinement," *Phys. Rev. Lett.* **48**(5), 322 (1982).
- <sup>104</sup>S. Murakami, H. Yamada, M. Sasao, M. Isobe, T. Ozaki, T. Saida, P. Goncharov, J. F. Lyon, M. Osakabe, T. Seki, Y. Takeiri, Y. Oka, K. Tumori, K. Ikeda, T. Mutoh, R. Kumazawa, K. Saito, Y. Torii, T. Watari, A. Wakasa, K. Y. Watanabe, H. Funaba, M. Yokoyama, H. Maassberg, C. D. Beidler, A. Fukuyama, K. Itoh, K. Ohkubo, O. Kaneko, A. Komori, O. Motojima, and LHD Experimental Group, "Effect of neoclassical transport optimization on energetic ion confinement in LHD," *Fusion Sci. Technol.* **46**, 241 (2004).
- <sup>105</sup>H. W. Kugel, D. Spong, R. Majeski, and M. Zarnstorff, *Fusion Sci. Technol.* **51**, 203 (2007).
- <sup>106</sup>S. Gori, J. Nührenberg, R. Zille, S. Okamura, K. Matsuoka, and S. Murakami, "Alpha-particle confinement optimization in quasi-axisymmetric configurations," *Plasma Phys. Controlled Fusion* **43**(2), 137–144 (2001).
- <sup>107</sup>M. I. Mikhailov, V. D. Shafranov, A. A. Subbotin, M. Y. Isaev, J. Nührenberg, R. Zille, and W. A. Cooper, "Improved  $\alpha$ -particle confinement in stellarators with poloidally closed contours of the magnetic field strength," *Nucl. Fusion* **42**, L23–L26 (2002).
- <sup>108</sup>A. V. Zvonkov, A. Y. Kuyanov, J. Nührenberg, A. A. Skvoroda, and R. Zille, "Toroidal mirror system," *Plasma Phys. Rep.* **28**(9), 756–764 (2002).
- <sup>109</sup>M. Drevlak, J. Geiger, P. Helander, and Y. Turkin, "Fast particle confinement with optimized coil currents in the W7-X stellarator," *Nucl. Fusion* **54**, 073002 (2014).
- <sup>110</sup>K. Ogawa, M. Isobe, K. Toi, A. Shimizu, D. A. Spong, M. Osakabe, S. Yamamoto, and LHD Experiment Group, "Energetic ion losses caused by magnetohydrodynamic activity resonant and non-resonant with energetic ions in large helical device," *Plasma Phys. Controlled Fusion* **56**, 094005 (2014).
- <sup>111</sup>K. Ogawa, M. Isobe, K. Toi, A. Shimizu, D. A. Spong, M. Osakabe, S. Yamamoto, and LHD Experiment Group, "A study on the TAE-induced fast-ion loss process in LHD," *Nucl. Fusion* **53**, 053012 (2013).
- <sup>112</sup>J. K. Anderson, A. F. Almagri, D. J. Den Hartog, S. Eilerman, C. B. Forest, J. J. Koliner, V. V. Mirnov, L. A. Morton, M. D. Nornberg, E. Parke, J. A. Reusch, J. S. Sarff, J. Waksman, V. Belykh, V. I. Davydenko, A. A. Ivanov, S. V. Polosatkin, Y. A. Tsidulko, L. Lin, D. Liu, G. Fiksel, H. Sakakita, D. A. Spong, and J. Titus, "Fast ion confinement and stability in a neutral beam injected reversed field pinch," *Phys. Plasmas* **20**(5), 056102 (2013).
- <sup>113</sup>J. K. Anderson, W. Capecchi, S. Eilerma, J. J. Koliner, M. D. Nornberg, J. A. Reusch, J. S. Sarff, and L. Lin, "Fast ion confinement in the three-dimensional helical reversed-field pinch," *Plasma Phys. Controlled Fusion* **56**, 094006 (2014).
- <sup>114</sup>P. Helander and D. J. Sigmar, *Collisional Transport in Magnetized Plasmas*, Cambridge Monographs on Plasma Physics Vol. 4 (Cambridge University Press, Cambridge, 2002).
- <sup>115</sup>W. I. van Rij and S. P. Hirshman, *Phys. Fluids B* **1**, 563 (1989).
- <sup>116</sup>V. V. Nemov, S. V. Kasilov, W. Kernbichler, and M. F. Heyn, "Evaluation of  $1/v$  neoclassical transport in stellarators," *Phys. Plasmas* **6**(12), 4622–4632 (1999).
- <sup>117</sup>J. Lore, W. Guttenfelder, A. Briesemeister, D. T. Anderson, F. S. B. Anderson, C. B. Deng, K. M. Likin, D. A. Spong, J. N. Talmadge, and K. Zhai, "Internal electron transport barrier due to neoclassical ambipolarity in the helically symmetric experiment," *Phys. Plasmas* **17**, 056101 (2010).
- <sup>118</sup>U. Stroth, K. Itoh, S.-L. Itoh, H. Hartfuss, and H. Laqua, "Internal transport barrier triggered by neoclassical transport in W7-AS," *Phys. Rev. Lett.* **86**(26), 5910–5913 (2001).
- <sup>119</sup>H. Maassberg, C. D. Beidler, U. Gasparino, M. Rome, K. S. Dyabilin, N. B. Marushchenko, and S. Murakami, "The neoclassical "Electron Root" feature in the Wendelstein-7-AS stellarator," *Phys. Plasmas* **7**(1), 295–311 (2000).
- <sup>120</sup>R. Burhenn, Y. Feng, K. Ida, H. Maassberg, K. J. McCarthy, D. Kalinina, M. Kobayashi, S. Morita, Y. Nakamura, H. Nozato, S. Okamura, S. Sudo, C. Suzuki, N. Tamura, A. Weller, M. Yoshinuma, and B. Zurro, "On impurity handling in high performance stellarator/heliotron plasmas," *Nucl. Fusion* **49**(6), 065005–8 (2009).
- <sup>121</sup>L. M. Kovrizhnykh, "Review: Neoclassical theory of transport processes in toroidal magnetic confinement systems, with emphasis on non-axisymmetric configurations," *Nucl. Fusion* **24**, 851 (1984).
- <sup>122</sup>C. D. Beidler and W. D. D'haeseleer, *Plasma Phys. Controlled Fusion* **37**, 463 (1995).
- <sup>123</sup>V. Tribaldos, "Monte Carlo estimation of neoclassical transport for the TJ-II stellarator," *Phys. Plasmas* **8**(4), 1229–1239 (2001).
- <sup>124</sup>M. Y. Isaev, S. Brunner, W. A. Cooper, T. M. Tran, A. Bergmann, C. D. Beidler, J. Geiger, H. Maassberg, J. Nührenberg, and M. Schmidt, *Fusion Sci. Technol.* **50**, 440 (2006).
- <sup>125</sup>C. D. Beidler, K. Allmeier, M. Y. Isaev, S. V. Kasilov, W. Kernbichler, G. O. Leitold, H. Maassberg, D. R. Mikkelsen, S. Murakami, M. Schmidt, S. A. Spong, V. Tribaldos, and A. Wakasa, "Benchmarking of the monoenergetic transport coefficients-results from the international collaboration on neoclassical transport in stellarators (ICNTS)," *Nucl. Fusion* **51**, 076001 (2011).

- <sup>126</sup>M. Taguchi, *Phys. Fluids B* **4**, 3638 (1992).
- <sup>127</sup>H. Sugama and S. Nishimura, "How to calculate the neoclassical viscosity, diffusion, and current coefficients in general toroidal plasmas," *Phys. Plasmas* **9**(11), 4637 (2002).
- <sup>128</sup>S. Nishimura and H. Sugama, "Neoclassical transport including impurities and the bootstrap current in advanced helical systems," *Fusion Sci. Technol.* **46**(1), 77–81 (2004).
- <sup>129</sup>H. Sugama, T. H. Watanabe, M. Nunami, and S. Nishimura, "Momentum balance and radial electric fields in axisymmetric and nonaxisymmetric toroidal plasmas," *Plasma Phys. Controlled Fusion* **53**(2), 024004–17 (2011).
- <sup>130</sup>D. A. Spong, "Generation and damping of neoclassical plasma flows in stellarators," *Phys. Plasmas* **12**, 056114 (2005).
- <sup>131</sup>D. A. Spong, J. H. Harris, A. S. Ware, S. P. Hirshman, and L. A. Berry, "Shear flow generation in stellarators—Configurational variations," *Nucl. Fusion* **47**(7), 626–633 (2007).
- <sup>132</sup>A. S. Ware, D. A. Spong, L. A. Berry, S. P. Hirshman, and J. F. Lyon, "Bootstrap current in quasi-symmetric stellarators," *Fusion Sci. Technol.* **50**(2), 236–244 (2006).
- <sup>133</sup>M. Landreman, H. M. Smith, A. Mollén, and P. Helander, "Comparison of particle trajectories and collision operators for collisional transport in nonaxisymmetric plasmas," *Phys. Plasmas* **21**, 042503 (2014).
- <sup>134</sup>M. Landreman, "The monoenergetic approximation in stellarator neoclassical calculations," *Plasma Phys. Controlled Fusion* **53**, 082003 (2011).
- <sup>135</sup>J. M. Garcia-Regana, R. Kleiber, C. D. Beidler, Y. Turkin, H. Maassberg, and P. Helander, "On neoclassical impurity transport in stellarator geometry," *Plasma Phys. Controlled Fusion* **55**, 074008 (2013).
- <sup>136</sup>K. C. Shaing, "Superbanana and superbanana plateau transport in finite aspect ratio tokamaks with broken symmetry," *J. Plasma Phys.* **81**(2), 905810203–12 (2014).
- <sup>137</sup>J. D. Callen, A. J. Cole, and C. C. Hegna, "Magnetic-perturbation-induced plasma transport in H-mode pedestals," *Phys. Plasmas* **19**, 112505 (2012).
- <sup>138</sup>D. del-Castillo-Negrete and L. Chacón, "Parallel heat transport in integrable and chaotic magnetic fields," *Phys. Plasmas* **19**, 056112 (2012).
- <sup>139</sup>D. Blazevski and D. del-Castillo-Negrete, "Local and nonlocal anisotropic transport in reversed magnetic fields: Shearless Cantori and nondifusive transport," *Phys. Rev. E* **87**, 063106 (2013).
- <sup>140</sup>D. del-Castillo-Negrete and D. Blazevski, "Heat pulse propagation in chaotic three-dimensional magnetic fields," *Nucl. Fusion* **54**, 064009 (2014).
- <sup>141</sup>A. Weller, D. A. Spong, R. Jaenicke, A. Lazaros, F. P. Penningsfeld, and S. Sattler, "Neutral beam driven global Alfvén eigenmodes in the Wendelstein W7-AS stellarator," *Phys. Rev. Lett.* **72**(8), 1220–1223 (1994).
- <sup>142</sup>M. Isobe, K. Toi, H. Matsushita, K. Goto, C. Suzuki, K. Nagaoka, N. Nakajima, S. Yamamoto, S. Murakami, A. Shimizu, Y. Yoshimura, T. Akiyama, T. Minami, M. Nishiura, S. Nishimura, D. S. Darrow, D. A. Spong, K. Shinohara, M. Sasao, K. Matsuoka, and S. Okamura, "Studies of fast-ion transport induced by energetic particle modes using fast-particle diagnostics with high time resolution in CHS," *Nucl. Fusion* **46**(10), S918–S925 (2006).
- <sup>143</sup>K. Toi, M. Isobe, M. Osakabe, F. Watanabe, K. Ogawa, S. Yamamoto, N. Nakajima, D. A. Spong, K. Ida, T. Ido, T. Ito, S. Morita, K. Nagaoka, K. Narihara, M. Nishiura, S. Ohdachi, S. Sakakibara, A. Shimizu, K. Tanaka, Y. Todo, T. Tokuzawa, and A. Weller, "MHD modes destabilized by energetic ions on LHD," *Fusion Sci. Technol.* **58**(1), 186–193 (2010).
- <sup>144</sup>A. V. Melnikov, M. Ochando, E. Ascasibar, F. Castejon, A. Cappa, L. G. Eliseev, C. Hidalgo, L. I. Krupnik, A. Lopez-Fraguas, M. Liniers, S. E. Lysenko, J. L. De Pablos, S. V. Perfilov, S. E. Sharapov, D. A. Spong, J. A. Jimenez, M. V. Ufimtsev, and B. N. Breizman, "Effect of magnetic configuration on frequency of NBI-driven Alfvén modes in TJ-II," *Nucl. Fusion* **54**(12), 123002 (2014).
- <sup>145</sup>D. G. Pretty and B. D. Blackwell, "A data mining algorithm for automated characterisation of fluctuations in multichannel time series," *Comput. Phys. Commun.* **180**, 1768–1776 (2009).
- <sup>146</sup>S. Yamamoto, D. Pretty, B. Blackwell, K. Nagasaki, H. Okada, F. Sano, T. Mizuchi, S. Kobayashi, K. Kondo, R. Jimenez-Gomez, E. Ascasibar, K. Toi, and S. Ohdachi, "Studies of MHD stability using data mining technique in helical plasmas," *Plasma Fusion Res.* **5**, 034–7 (2010).
- <sup>147</sup>C. B. Deng, D. L. Brower, B. N. Breizman, D. A. Spong, A. F. Almagri, D. T. Anderson, F. S. B. Anderson, W. X. Ding, W. Guttenfelder, K. M. Likin, and J. N. Talmadge, "Energetic-electron-driven instability in the helically symmetric experiment," *Phys. Rev. Lett.* **103**(2), 025003 (2009).
- <sup>148</sup>J. J. Koliner, C. B. Forest, J. S. Sarff, J. K. Anderson, D. Liu, M. D. Nornberg, J. Waksman, L. Lin, D. L. Brower, W. X. Ding, and D. A. Spong, "Fast-particle-driven alfvénic modes in a reversed field pinch," *Phys. Rev. Lett.* **109**(11), 115003 (2012).
- <sup>149</sup>D. A. Spong, R. Sanchez, and A. Weller, "Shear Alfvén continua in stellarators," *Phys. Plasmas* **10**, 3217–3224 (2003).
- <sup>150</sup>D. A. Spong, E. D'Azevedo, and Y. Todo, *Phys. Plasmas* **17**, 022106 (2010).
- <sup>151</sup>A. Könies and D. Eremin, "Coupling of Alfvén and sound waves in stellarator plasmas," *Phys. Plasmas* **17**(1), 012107 (2010).
- <sup>152</sup>W. A. Cooper, G. Y. Fu, S. Gruber, S. Merazzi, U. Schwenn, and D. V. Anderson, in *Proceedings of the Joint Varenna- Lausanne International Workshop on Theory of Fusion Plasmas, Varenna, Italy, 1990* (Editrice Compositori, Bologna, Italy, 1990), p. 655.
- <sup>153</sup>K. Toi *et al.*, in *Proceedings of the 22nd IAEA Fusion Energy Conference*, Paper No. EX/P8-4, Geneva (2009).
- <sup>154</sup>A. V. Melnikov, L. G. Eliseev, E. Ascasibar, A. A. Chmyga, C. Hidalgo, T. Ido, R. Jimenez-Gomez, A. D. Komarov, A. S. Kozachek, L. I. Krupnik, S. M. Khrebtov, A. Könies, Y. K. Kuznetsov, A. Lopez-Fraguas, S. E. Lysenko, V. A. Mavrin, K. Nagaoka, J. L. de Pablos, M. A. Pedrosa, S. V. Perfilov, A. I. Smolyakov, D. A. Spong, M. V. Ufimtsev, and S. Yamamoto, "Alfvén eigenmode properties and dynamics in the TJ-II stellarator," *Nucl. Fusion* **52**(12), 123004–9 (2012).
- <sup>155</sup>Y. I. Kolesnichenko, V. V. Lutsenko, H. Wobig, and V. Yakovenko, "Alfvén instabilities driven by circulating ions in optimized stellarators and their possible consequences in a Helias reactor," *Phys. Plasmas* **9**(2), 517–528 (2002).
- <sup>156</sup>A. Konies, "A kinetic magnetohydrodynamic energy integral in three dimensional geometry," *Phys. Plasmas* **7**(4), 1139–1147 (2000).
- <sup>157</sup>C. Nührenberg, *Phys. Plasmas* **6**, 137 (1999).
- <sup>158</sup>D. A. Spong, B. N. Breizman, D. L. Brower *et al.*, *Contrib. Plasma Phys.* **50**, 708 (2010).
- <sup>159</sup>M. Y. Isaev, S. Y. Medvedev, S. D. Pinches, and S. E. Sharapov, "Nonlinear saturation of the Toroidal Alfvén Eigenmodes computed with the VENUS +  $\delta f$ , HAGIS, and KINX codes," in *Proceedings of the 40th EPS Conference on Plasma Physics, EPS* (2013), Vol. 1, pp. 389–392.
- <sup>160</sup>A. Mishchenko, A. Könies, T. Fehér, R. Kleiber, M. Borchardt, J. Riemann, R. Hatzky, J. Geiger, and Y. Turkin, "Global hybrid-gyrokinetic simulations of fast-particle effects on Alfvén Eigenmodes in stellarators," *Nucl. Fusion* **54**, 104003 (2014).
- <sup>161</sup>Y. Todo, "Simulations of Alfvén eigenmodes with an extended Ohm's law," *J. Plasma Phys.* **72**(6), 817–820 (2006).
- <sup>162</sup>I. Holod and D. A. Spong, "Extension of GTC capability for simulating non-axisymmetric systems," *Bull. Am. Phys. Soc.* **59**(15), 369 (2014).
- <sup>163</sup>D. A. Spong, "Three-dimensional effects on energetic particle confinement and stability," *Phys. Plasmas* **18**, 056109 (2011).
- <sup>164</sup>A. Bortolon, W. W. Heidbrink, G. J. Kramer, J.-K. Park, E. D. Fredrickson, J. D. Lore, and M. Podesta, "Mitigation of Alfvén activity in a tokamak by externally applied static 3D fields," *Phys. Rev. Lett.* **110**(26), 265008-5 (2013).
- <sup>165</sup>A. Bortolon, W. W. Heidbrink, G. J. Kramer, J.-K. Park, E. D. Fredrickson, M. Podesta, N. M. Ferraro, J. D. Lore, D. A. Spong, and NSTX Team, "Mitigation of Alfvénic activity by 3D magnetic perturbations on NSTX," Invited talk, in *Proceedings of the 41st EPS Conference, Berlin, Germany, 23–27 June (2014)*.
- <sup>166</sup>H. Yamada, K. Ida, S. Murakami, K. Y. Watanabe, E. Ascasibar, R. Brakel, A. Dinklage, J. H. Harris, S. Okamura, F. Sano, U. Stroth, S. Inagaki, K. Tanaka, M. Goto, K. Nishimura, K. Narihara, S. Morita, S. Sakakibara, B. J. Peterson, R. Sakamoto, J. Miyazawa, T. Morisaki, M. Osakabe, K. Toi, N. Tamura, K. Ikeda, K. Yamazaki, K. Kawahata, O. Kaneko, N. Ohyabu, A. Komori, and O. Motojima, "Configuration effect on energy confinement and local transport in LHD and contribution to the international stellarator database," *Fusion Sci. Technol.* **46**(1), 82–90 (2004).
- <sup>167</sup>A. Dinklage, M. Yokoyama, K. Tanaka, J. L. Velasco, D. López-Bruna, C. D. Beidler, S. Satake, E. Ascasibar, J. Arévalo, J. Baldzuhn, Y. Feng, D. Gates, J. Geiger, K. Ida, M. Isaev, M. Jakubowski, A. López-Fraguas, H. Maaberg, J. Miyazawa, T. Morisaki, S. Murakami, N. Pablant, S. Kobayashi, R. Seki, C. Suzuki, Y. Suzuki, Y. Turkin, A. Wakasa, R. Wolf, H. Yamada, and M. Yoshinuma, "Inter-machine validation study of neoclassical transport modelling in medium- to high-density stellarator-helion plasma," *Nucl. Fusion* **53**(6), 063022 (2013).

- <sup>168</sup>G. Rewoldt, L.-P. Ku, and W. M. Tang, *Phys. Plasmas* **12**, 102512 (2005).
- <sup>169</sup>P. Xanthopoulos, F. Merz, T. Gorler, and F. Jenko, “Nonlinear gyrokinetic simulations of ion-temperature-gradient turbulence for the optimized Wendelstein 7-X stellarator,” *Phys. Rev. Lett.* **99**(3), 035002-1–4 (2007).
- <sup>170</sup>H. Mynick, P. Xanthopoulos, B. Faber, M. Lucia, M. Rorvig, and J. N. Talmadge, “Turbulent optimization of toroidal configurations,” *Plasma Phys. Controlled Fusion* **56**, 094001 (2014).
- <sup>171</sup>P. Xanthopoulos, H. E. Mynick, P. Helander, Y. Turkin, G. G. Plunk, F. Jenko, T. Görler, D. Told, T. Bird, and J. H. E. Proll, “Controlling turbulence in present and future stellarators,” *Phys. Rev. Lett.* **113**, 155001 (2014).
- <sup>172</sup>H. E. Mynick, N. Pomphrey, and S. Ethier, “Exploration of stellarator configuration space with global search methods,” *Phys. Plasmas* **9**(3), 869–876 (2002).
- <sup>173</sup>P. B. Snyder, H. R. Wilson, J. R. Ferron, L. L. Lao, A. W. Leonard, T. H. Osborne, A. D. Turnbull, D. Mossessian, M. Murakami, and X. Q. Xu, “Edge localized modes and the pedestal: A model based on coupled peeling-balloonning modes,” *Phys. Plasmas* **9**, 2037–2043 (2002).
- <sup>174</sup>E. Strumberger, S. Günter, P. Merkel, E. Schwarz, and C. Tichmann, “MHD instabilities in 3D tokamaks,” *Nucl. Fusion* **50**, 025008 (2010).
- <sup>175</sup>T. Weyens, R. Sánchez, L. García, A. Loarte, and G. Huijsmans, “Three-dimensional linear peeling-balloonning theory in magnetic fusion devices,” *Phys. Plasmas* **21**, 042507 (2014).
- <sup>176</sup>G. Y. Fu, M. Isaev, L. P. Ku, M. Mikhailov, M. H. Redi, R. Sanchez, A. Subbotin, W. A. Cooper, S. P. Hirshman, D. A. Monticello, A. Reiman, and M. Zarnstorff, “Ideal magnetohydrodynamic stability of the NCSX,” *Fusion Sci. Technol.* **51**(2), 218 (2007).
- <sup>177</sup>C. Mercier, “MHD stability criteria for localized displacements,” *Plasma Phys.* **21**(7), 589–612 (1979).
- <sup>178</sup>R. Sanchez, S. P. Hirshman, J. C. Whitson, and A. S. Ware, “COBRA: An optimized code for fast analysis of ideal ballooning stability of three-dimensional magnetic equilibria,” *J. Comput. Phys.* **161**(2), 576–588 (2000).
- <sup>179</sup>G. Y. Fu, W. A. Cooper, R. Gruber, U. Schwenn, and D. V. Anderson, “Fully three-dimensional ideal magnetohydrodynamic stability analysis of low-n modes and Mercier modes in stellarators,” *Phys. Fluids B* **4**(6), 1401–1411 (1992).
- <sup>180</sup>K. Ichiguchi and B. A. Carreras, “Multi-scale MHD analysis incorporating pressure transport equation for beta-increasing LHD plasma,” *Nucl. Fusion* **51**, 053021–7 (2011).
- <sup>181</sup>J. Varela, K. Y. Watanabe, S. Ohdachi, and Y. Narushima, “Hard magnetohydrodynamic limit in 1/3 sawtooth like activity in LHD,” *Phys. Plasmas* **21**, 032501 (2014).
- <sup>182</sup>H. Yamada, K. Y. Watanabe, S. Sakakibara, Y. Suzuki, S. Ohdachi, M. Kobayashi, H. Funaba, and LHD Experiment Group, “Study of high-beta plasmas in a helical system,” *Contrib. Plasma Phys.* **50**(6–7), 480–486 (2010).
- <sup>183</sup>A. Weller, J. Geiger, A. Werner, M. C. Zarnstorff, C. Nührenberg, E. Sallander, J. Baldzuhn, R. Brakel, R. Burhenn, A. Dinklage, E. Fredrickson, F. Gadelmeier, L. Giannone, P. Grigull, D. Hartmann, R. Jaenicke, S. Klose, J. P. Knauer, A. Konies, Y. I. Kolesnichenko, H. P. Laqua, V. V. Lutsenko, K. McCormick, D. Monticello, M. Osakabe, E. Pasch, A. Reiman, N. Rust, D. A. Spong, F. Wagner, Y. V. Yakovenko, W7-AS Team, and NBI-Group, “Experiments close to the beta-limit in W7-AS,” *Plasma Phys. Controlled Fusion* **45**, A285–A308 (2003).
- <sup>184</sup>J. H. Harris, M. Murakami, B. A. Carreras, J. D. Bell, G. L. Bell, T. S. Bigelow, L. A. Charlton, N. Dominguez, J. L. Dunlap, J. C. Glowienka, L. D. Horton, H. C. Howe, R. C. Isler, H. Kaneko, R. R. Kindsfather, J. N. Leboeuf, V. E. Lynch, M. M. Menon, R. N. Morris, G. H. Neilson, V. K. Pare, D. A. Rasmussen, J. B. Wilgen, and W. R. Wing, “Second stability in the ATF torsatron,” *Phys. Rev. Lett.* **63**(12), 1249–1252 (1989).
- <sup>185</sup>A. S. Ware, S. P. Hirshman, D. A. Spong, L. A. Berry *et al.*, *Phys. Rev. Lett.* **89**, 125003 (2002).
- <sup>186</sup>S. Hudson, C. C. Hegna, R. Torasso, and A. S. Ware, *Plasma Phys. Controlled Fusion* **46**, 869 (2004).
- <sup>187</sup>G. J. Kramer, A. McLean, N. Brooks *et al.*, *Nucl. Fusion* **53**, 123018 (2013).
- <sup>188</sup>G. J. Kramer, B. V. Budny, R. Ellis *et al.*, *Nucl. Fusion* **51**, 103029 (2011).
- <sup>189</sup>K. Toi, *AIP Conf. Proc.* **1478**, 116–128 (2012).

Physics of Plasmas is copyrighted by AIP Publishing LLC (AIP). Reuse of AIP content is subject to the terms at: <http://scitation.aip.org/termsconditions>. For more information, see <http://publishing.aip.org/authors/rights-and-permissions>.